International Journal of Solids and Structures 222–223 (2021) 111017

Contents lists available at ScienceDirect

International Journal of Solids and Structures

journal homepage: www.elsevier.com/locate/ijsolstr

A new concept for the representative directions method: Directionalisation of first and second invariant based hyperelastic models

A.B. Aydogdu *, K. Loos, M. Johlitz, A. Lion

Institute of Mechanics, Universität der Bundeswehr München, Werner-Heisenberg-Weg 39, 85579 Neubiberg, Germany

ARTICLE INFO

Article history:
Received 23 September 2020
Received in revised form 8 February 2021
Accepted 2 March 2021
Available online 11 March 2021

Keywords:
Representative directions
Affine and non-affine
Directionalisation
Optimisation
Finite-element

ABSTRACT

The representative directions method is a continuum mechanical based practical approach to transfer 1D material models to 3D. The selection of the directional energy and the corresponding directional stress is generally based on the standard uniaxial tension (UT) solution of hyperelastic models. However, this approach results in a somewhat different model than hyperelastic models in the context of elasticity and inelasticity. For instance, enrichment of the UT based directional stress with the non-affine stretch does not provide close results unless huge p-root values are considered. Hence, the main objective of this contribution is to determine the directional stresses, which can provide equivalent or close results to first and second invariant based hyperelastic models. Accordingly, the directionalisation concept in the framework of affine representative directions method is introduced. Directional stresses are obtained with a top-down approach from the first and second invariant based hyperelastic models. The standard Mooney-Rivlin model is directionalised to obtain the corresponding 1D energies and stresses using the micro-stretch and the macro-area-stretch. The approach is then utilised to directionalise several hyperelastic-like models as alternatives for statistical-thermomechanics based chain models. Moreover, a new optimisation strategy is proposed to improve the material asymmetry resulting from numerical integration schemes. Optimisation results demonstrate that the material symmetry of the standard Bažant points can be improved. Finally, two nonhomogenous finite-element (FE) simulations demonstrate that the directionalisation approach presented here contributes a good step towards numerically robust inelastic extensions.

1. Introduction

Rubbery, biological and metallic materials generally depict process induced anisotropies when subjected to mechanical and thermal loadings. To capture initial anisotropy and deformation induced anisotropies, typical and plausible methods to consider are the so-called microplane, affine and non-affine microsphere, and representative directions model depending on the application area. Historically, the microplane model dates back to the works of Bažant (1984), Bažant and Gambarova (1984), Bažant and Oh (1985) in connection to capture inelastic effects in concrete and rocks. One of the first thermodynamically consistent approaches in this field in a small-strain framework was introduced by the authors (Carol et al., 2001; Kuhl et al., 2001). Further on, Carol et al. (2004) has extended the microplane modelling to the large strain framework with an emphasis on hyperelasticity. To the best of authors' knowledge, one of the first contribution to the microsphere approach is the work of Pawelski (1998) in the context of elastomers. Later on, the so-called microsphere approaches were further developed for modelling the viscoelasticity and the Mullins effect observed in rubbery polymers with three consecutive contributions by Miehe et al. (2004), Miehe and Göktepe (2005), Göktepe and Miehe (2005). To clarify, as described in Freund and Ihlemann (2010), the difference between the microsphere and the representative direction method is solely based on the consideration of the statistical mechanics with a proper homogenisation technique and a continuum mechanical approach, respectively. As a matter of fact, all three modelling approaches are similar, but the physical reasoning of 1D models and their application fields are somewhat different. In any case, the most obvious advantage of both approaches is that a proper 1D constitutive model can be transferred to 3D effortlessly, as developing a 1D model is relatively

* Corresponding author.
E-mail addresses: ahmet.aydogdu@unibw.de (A.B. Aydogdu), alexander.lion@unibw.de (A. Lion).

https://doi.org/10.1016/j.ijsolstr.2021.03.004
0020-7683/

simpler than tensor invariant based 3D models. In general, except for modelling concrete, rock and soil materials, the microsphere models are more popular; therefore, there exist numerous contributions for the last 20 years. For example, for modelling rubber-like materials, Dal and Kaliske (2009), Dal et al. (2018a), Dal et al. (2018b) applied this approach in the context of ageing and viscoplasticity of uncured green rubber. Furthermore, recent treatment of Berger and Kaliske (2020) for rubber curing is also referred. Another important application area is strain-induced crystallisation in elastomers. The reader is referred to works of Mistry and Govindjee (2014), Guilié et al. (2015), Nateghi et al. (2018) and representative directions approach of Loos et al. (2020), Loos et al. (2020). In analogy to rubbery materials, biological materials experience deformation-induced anisotropies due to their collagen microstructure, for instance, numerous contributions were published by Menzel and Waffenschmidt (2009), Waffenschmidt et al. (2014) and Thylander et al. (2017) for biologic materials. In the context of metallic materials, more recently, the microsphere approach was also considered for modelling the anisotropic behaviour of metallic foams by Bleistein et al. (2020).

In the context of the representative directions method, the fundamental question to answer is the selection of the 1D strain energy density and the stress-stretch relationship. In the contribution of Lion et al. (2013), the homogeneous UT form of the 2 parameter Mooney-Rivlin model was employed in each direction and was analytically integrated. The analytical results demonstrated that the stress response of the directional approach is considerably softer than the corresponding UT solution. Based on this observation, the p-root averaging technique of Miehe et al. (2004) has been further included and compared with the original solutions of Lion et al. (2013). Except for high p values, the approach does not provide close results. Therefore, the main purpose of this contribution is the introduction of the directionalisation concept. The term directionalisation means that the directional stress is defined along each direction vector in the unit-sphere, yet the sum over all these directions should return the original stress tensor of the selected hyperelastic model. The directionalisation approach is quite significant in three aspects. First, when analytically integrated, it should provide exactly the same stress response with its own 3D invariant based form, thus eliminating the numerical integration. Second, it provides a phenomenological one-to-one alternative to statistical physics based micromechanical constitutive laws of the microsphere model. Third, the directionalisation will hold the numerical properties of the original hyperelastic model, as further inelastic extensions could make the convergence matters worse in FE analyses. Within this perspective, the reader is referred to Dal et al. (2018b) for discussions about the so-called strong ellipticity and the convexity of the microsphere models. For a detailed introdution for the strong ellipticity, the reader is referred to the works of Marsden and Hughes (1994), Antman (1995) and Walton and Wilber (2003).

In the context of large strains and microplane approach, Carol et al. (2004) introduced a directional model for the compressible Mooney-Rivlin model. To do this, in addition to the microplane stretch, the so-called microplane thickening were utilised for the directional version of the second invariant of the right Cauchy-Green deformation tensor. Furthermore, the Jacobian were also included in the directional form of the Mooney-Rivlin strain energy density by Carol et al. (2004). In the work of Verron (2015), the directional potential of the Mooney-Rivlin model was obtained in terms of the microplane stretch only. In this study, two different stretch measures will be used to directionalise the second invariant of the unimodular right Cauchy-Green deformation tensor.

Another important aspect of the directional models is the analytical or numerical integration of 1D constitutive laws on the unit-sphere. In general, analytical integration is not possible. Accordingly, the mostly employed integration points in the literature are based on the integration directions and weights of Bažant and Oh (1986), particularly the scheme using 21 integration points. These integration directions and weights are of Gauss type with an optimal distribution on the sphere rather than the rectangular domain. For instance, there are also several different sets of integration points computed, such as Fliege and Maier (1999). For a detailed comparison of different strategies, a reference is made to Itskov (2016) and Verron (2015) for further discussions about the efficiency of the integration points of Bažant and Oh (1986). In numerical integration schemes, the material symmetry must be ensured. This particularly means that when the same load is applied in each direction of the unit-sphere, no artificial material asymmetry should arise in the case of initial isotropy. In the work of Ehret et al. (2010), arbitrary rigid rotations were applied on many different integration schemes and their performance were compared with the so-called Akaike information criterion. Based on this observations, we attempt to provide an ad hoc algorithm to improve the artificial material asymmetry arising due to integration schemes. In detail, any UT, equibiaxial tension (ET), or pure shear (PS) experimental data; or even the solutions of hyperelastic models for these experiments could be used as a basis to improve the symmetry issues related to any numerical integration scheme. The algorithm is based on a rotational scheme, which rotates all integration directions on the choosen coordinate system of the UT, ET, or PS case. In simple words, for n number of directions, n number of rotations should be done. Eventually, the aim is to load the unit-sphere in all discrete directions possible and compute an error function to minimise. As an example, the widely used 21 point integration scheme of Bažant (1984) is employed and investigated.

The organisation of the paper is as follows: the thermodynamically consistent continuum mechanical framework for the affine and non-affine representative directions approach is formulated in Section 2. Furthermore, the directionalisation concept and ad hoc algorithm for the optimisation of the integration weights are introduced. Section 3 illustrates the comparisons between the numerical and exact solutions of Lion et al. (2013) for the UT and the ET, the parameter identification of the models and improvement of the material symmetry of Bažant and Oh (1986)'s 21 integration points. Moreover, two FE benchmarks are considered to compare several directional stresses described in Section 2. Finally, Section 4 summarises the study with an overview and concluding remarks.

2. The mathematical model

In this section, the continuum mechanical framework based on the hybrid free energy approach published by Lion et al. (2014) will be followed. For the continuum mechanical basics, the reader is referred to Haupt (2000). Herein, a multiplicative decomposition of the deformation gradient into isochoric and volumetric parts in the sense of Flory (1961) is considered.

2.1. Kinematics

The deformation gradient $\mathbf{F}$ is multiplicatively split into two parts: an isochoric $\hat{\mathbf{F}} = J^{-1/3}\,\mathbf{F}$ and a volumetric $\bar{\mathbf{F}} = J^{1/3}\,\mathbf{I}$ part such that

$$\mathbf{F} = \hat{\mathbf{F}} \cdot \bar{\mathbf{F}} \text{ with } J = \det \mathbf{F}. \tag{1}$$

The isochoric deformation gradient $\hat{\mathbf{F}}$ has the property of $\det \hat{\mathbf{F}} = 1$. Consequently, the isochoric right Cauchy-Green deformation tensor based on Eq. (1) can be expressed as

$$\hat{\mathbf{C}} = \hat{\mathbf{F}}^T \cdot \hat{\mathbf{F}} = J^{-\frac{2}{3}} \mathbf{F}^T \cdot \mathbf{F} = J^{-\frac{2}{3}} \mathbf{C}. \tag{2}$$

Furthermore, the time rate of $\hat{\mathbf{C}}$ is given as

$$\dot{\hat{\mathbf{C}}} = \overset{4}{\mathbf{P}} : \dot{\mathbf{C}}, \tag{3}$$

where $\overset{4}{\mathbf{P}} = J^{-\frac{2}{3}}\left(\mathbf{I} - \frac{1}{3}\,\mathbf{C}\otimes\mathbf{C}^{-1}\right)$ is the fourth order projection tensor.

2.2. Affine and non-affine representative directions method

In parallel with the study of Lion et al. (2013), the direction vector is given as

$$\mathbf{e}_\alpha = \sin\vartheta\,\cos\varphi\,\mathbf{e}_1 + \sin\vartheta\,\sin\varphi\,\mathbf{e}_2 + \cos\vartheta\,\mathbf{e}_3. \tag{4}$$

Fig. 1 illustrates the spherical coordinates and the direction vector $\mathbf{e}_\alpha$ given in Eq. (4). For the affine model, see Miehe et al. (2004) and Lion et al. (2013), the isochoric micro-stretch reads as

$$\hat{\lambda}_\alpha = \sqrt{\mathbf{e}_\alpha\cdot\hat{\mathbf{C}}\cdot\mathbf{e}_\alpha} = \sqrt{\mathbf{e}_\alpha\otimes\mathbf{e}_\alpha : \hat{\mathbf{C}}}. \tag{5}$$

The isochoric micro-stretch $\hat{\lambda}_\alpha$ or any other thermodynamical quantity has to be integrated on the unit-sphere by the given relationship

$$f_{\text{avg}}(t) = A[f_\alpha(\mathbf{e}_\alpha, t)] = \frac{1}{4\pi}\int_0^{2\pi}\int_0^{\pi} f_\alpha(\mathbf{e}_\alpha, t)\,\mathrm{d}\Omega, \tag{6}$$

where $\mathrm{d}\Omega = \sin\vartheta\,\mathrm{d}\vartheta\,\mathrm{d}\varphi$. The operator A in Eq. (6) is a shorthand notation for the exact integration. Next, based on Miehe et al. (2004), the p-root averaging operator is defined as

$$f^s_{\text{avg}}(t) = \left(A\left[f_\alpha(\mathbf{e}_\alpha, t)^s\right]\right)^{1/s}. \tag{7}$$

The main motivation behind the non-affine model of Miehe et al. (2004) is that the polymer chains have deformation capabilities up to some physical limit. Therefore, p-root averaging (here denoted as s to avoid notational confusion with the pressure p) implies additional stiffness in comparison with the affine model. Consequently, the micro-stretch for the non-affine model follows as

$$\hat{\lambda} = \left(A\left[\hat{\lambda}^s_\alpha\right]\right)^{1/s}. \tag{8}$$

Due to thermomechanical considerations, the rates of micro-stretches are needed. First, the rate of the affine isochoric stretch $\hat{\lambda}_\alpha$ in Eq. (5) is given by

$$\dot{\hat{\lambda}}_\alpha = \frac{1}{\hat{\lambda}_\alpha}\,\mathbf{e}_\alpha\otimes\mathbf{e}_\alpha : \frac{1}{2}\,\dot{\hat{\mathbf{C}}}. \tag{9}$$

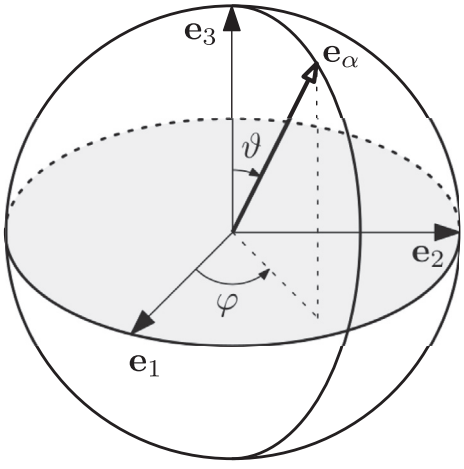

Fig. 1. Representative directions and the coordinates.

Likewise, the rate of the non-affine isochoric micro-stretch can be computed as

$$\dot{\hat{\lambda}} = A\left[\hat{\lambda}^{1-s}\,\hat{\lambda}^{s-2}_\alpha\,\mathbf{e}_\alpha\otimes\mathbf{e}_\alpha\right] : \frac{1}{2}\,\dot{\hat{\mathbf{C}}}. \tag{10}$$

The rates of stretches in Eq. (9) and Eq. (10) will be taken into account when acquiring the 2nd Piola–Kirchhoff (2nd PK) stress tensor $\mathbf{S}$ from the Clausius–Duhem inequality (CDI).

2.3. Thermodynamical consistency

In this study, the standard procedure of Noll and Coleman (1974) is applied in order to ensure thermodynamical consistency. To begin with, for the affine model, the specific hybrid free energy Φ is defined as

$$\Phi = \Phi^{vol}(p) + A\left[\Phi^{iso}_\alpha\left(\hat{\lambda}_\alpha\right)\right]. \tag{11}$$

Similarly, for the non-affine case, it is expressed as

$$\Phi = \Phi^{vol}(p) + \Phi^{iso}\left(\hat{\lambda}\right). \tag{12}$$

By making use of the time derivative of Eq. (11), the following form of the CDI for the affine case is written as

$$\mathbf{S} : \frac{1}{2}\,\dot{\mathbf{C}} + p\dot{J} - A\left[\hat{\sigma}_\alpha\,\dot{\hat{\lambda}}_\alpha\right] \geqslant 0 \text{ with} \tag{13}$$

$$\varepsilon_{vol} = \rho_R\,\frac{\partial\Phi^{vol}}{\partial p}, \tag{14}$$

where the directional stress is $\hat{\sigma}_\alpha = \rho_R\,\frac{\partial\Phi^{iso}}{\partial\hat{\lambda}_\alpha}$. Based on the considerations of Lion et al. (2013), the volumetric hybrid free energy density Φ^{vol} can be defined as

$$\rho_R\,\Phi^{vol} = -\frac{p^2}{2K}, \tag{15}$$

where K is the compression modulus. Using Eq. (3), the time rate of the Jacobian $\dot{J} = \frac{1}{2}J\mathbf{C}^{-1} : \dot{\mathbf{C}}$ and the rate of the affine isochoric micro-stretch in Eq. (9), the 2nd PK stress tensor from CDI Eq. (13) yields to

$$\mathbf{S} = -pJ\mathbf{C}^{-1} + A\left[\hat{\mathbf{S}}_\alpha\right], \tag{16}$$

and the directional isochoric stress tensor $\hat{\mathbf{S}}_\alpha$ is

$$\hat{\mathbf{S}}_\alpha = J^{-\frac{2}{3}}\left(\frac{\hat{\sigma}_\alpha}{\hat{\lambda}_\alpha}\,\mathbf{e}_\alpha\otimes\mathbf{e}_\alpha - \frac{1}{3}\,\hat{\sigma}_\alpha\,\hat{\lambda}_\alpha\hat{\mathbf{C}}^{-1}\right). \tag{17}$$

In the case of non-affinity, since the volumetric parts for both the affine and the non-affine cases are equal, the directional part of the 2nd PK stress tensor for the non-affine approach reads as

$$\hat{\mathbf{S}}_\alpha = J^{-\frac{2}{3}}\,\frac{\hat{\sigma}\hat{\lambda}^s_\alpha}{\hat{\lambda}^{s-1}}\left(\hat{\lambda}^{-2}_\alpha\,\mathbf{e}_\alpha\otimes\mathbf{e}_\alpha - \frac{1}{3}\,\hat{\mathbf{C}}^{-1}\right), \tag{18}$$

where the implicitly directional stress is $\hat{\sigma} = \rho_R\,\frac{\partial\Phi^{iso}}{\partial\hat{\lambda}}$.

2.4. Numerical integration of the representative directions

The affine isochoric micro-stretch $\hat{\lambda}_\alpha$ or any other directional quantity has to be integrated along each direction of the unit-sphere illustrated in Fig. 1. In general, analytical integration of the directional stresses $\hat{\sigma}_\alpha$ is not possible. To this end, numerical integration on the unit-sphere has to be employed. In a straightforward sense, these numerical integrations are weighted evaluations for the given number of directions:

$$A[f_\alpha] \approx AD[f_\alpha] = \sum_{\alpha=1}^{n_{\text{dir}}} w_\alpha f_\alpha, \tag{19}$$

where $AD[\cdots]$ is the discrete sum operator. Thus, the 2nd PK stress tensor can be expressed in a discrete form

$$\mathbf{S} = -pJ\mathbf{C}^{-1} + \sum_{\alpha=1}^{n_{\text{dir}}} w_\alpha \hat{\mathbf{S}}_\alpha. \tag{20}$$

Subsequently, the Cauchy stress tensor $\mathbf{T}$ can be obtained with the push-forward operation $\mathbf{T} = \frac{1}{J}\mathbf{F}\cdot\mathbf{S}\cdot\mathbf{F}^T$. Finally, the material tangent moduli $\mathbb{C}$ have to be computed. The relation to calculate the moduli $\mathbb{C}$ is given as

$$\mathbb{C} = 2\frac{\partial \mathbf{S}}{\partial \mathbf{C}} = \bar{\mathbb{C}} + A\left[\hat{\mathbb{C}}_\alpha\right], \tag{21}$$

where $\bar{\mathbb{C}}$ and $\hat{\mathbb{C}}_\alpha$ are the volumetric and the isochoric directional parts, respectively. Then, for the affine and non-affine case, the material tangent moduli are shown in Table 1. Table 1 demonstrates that both models have the same structure with the only difference between the isochoric material tangent modulus terms f_1, f_2, f_3 and f_4. The pressure p can be calculated from the mixed u-p approach described in Section 3.4.

2.5. Directional stresses for the Mooney-Rivlin type elasticity

For simple deformation cases such as the UT, the unidirectional (single direction) stress can be computed as

$$P_{ut} = 2\mu_1\left(\lambda - \frac{1}{\lambda^2}\right) + 2\mu_2\left(1 - \frac{1}{\lambda^3}\right). \tag{22}$$

Similarly, for the ET case, it reads as

$$P_{et} = 2\mu_1\left(\lambda - \frac{1}{\lambda^5}\right) + 2\mu_2\left(\lambda^3 - \frac{1}{\lambda^3}\right). \tag{23}$$

Based on the unidirectional solution of the UT in Eq. (22), Lion et al. (2013) considered the directional stresses for the affine case as

$$\hat{\sigma}_\alpha = 2\mu_1\left(\hat{\lambda}_\alpha - \frac{1}{\hat{\lambda}_\alpha^2}\right) + 2\mu_2\left(1 - \frac{1}{\hat{\lambda}_\alpha^3}\right). \tag{24}$$

Similarly, the non-affine stress $\hat{\sigma}$ can be defined as

$$\hat{\sigma} = 2\mu_1\left(\hat{\lambda} - \frac{1}{\hat{\lambda}^2}\right) + 2\mu_2\left(1 - \frac{1}{\hat{\lambda}^3}\right), \tag{25}$$

which is implicitly directional via $\hat{\lambda}$ in Eq. (8). Eq. (24) has to be computed for each representative direction. On the other hand, the non-affine stress in Eq. (25) is computed only once. The exact solutions of the 1st PK stress tensor resulting from Eq. (24) for the UT and the ET are not restated here as they are rather lengthy; therefore, the reader is referred to Lion et al. (2013).

Table 1
The material moduli for the affine and non-affine representative directions approach without internal variables.

i. Isochoric part:
$\hat{\mathbb{C}}_\alpha = -\frac{1}{3}J^{-\frac{2}{3}}f_1\,\mathbf{C}^{-1}\otimes\mathbf{e}_\alpha\otimes\mathbf{e}_\alpha + \mathbf{e}_\alpha\otimes\mathbf{e}_\alpha\otimes\mathbf{C}^{-1}$
$+J^{-\frac{4}{3}}f_2\,\mathbf{e}_\alpha\otimes\mathbf{e}_\alpha\otimes\mathbf{e}_\alpha\otimes\mathbf{e}_\alpha + \frac{1}{9}f_3\,\mathbf{C}^{-1}\otimes\mathbf{C}^{-1} - \frac{2}{3}f_4\,\frac{\partial\mathbf{C}^{-1}}{\partial\mathbf{C}}$
ii. Volumetric part:
$\bar{\mathbb{C}} = -pJ\mathbf{C}^{-1}\otimes\mathbf{C}^{-1} - 2pJ\,\frac{\partial\mathbf{C}^{-1}}{\partial\mathbf{C}}$
iii. Affine, non-affine:
$f_1 = \frac{\hat{\sigma}_\alpha}{\hat{\lambda}_\alpha} + \frac{\partial\hat{\sigma}_\alpha}{\partial\hat{\lambda}_\alpha}$, $\hat{\lambda}^{1-s}\hat{\lambda}_\alpha^{s-1}\,g_1$
$f_2 = \frac{1}{\hat{\lambda}_\alpha^2}\frac{\partial\hat{\sigma}_\alpha}{\partial\hat{\lambda}_\alpha} - \frac{\hat{\sigma}_\alpha}{\hat{\lambda}_\alpha^3}$, $\frac{\hat{\lambda}^{1-s}}{\hat{\lambda}_\alpha^{3-s}}\left(g_1 - 2\frac{\hat{\sigma}}{\hat{\lambda}_\alpha}\right)$
$f_3 = \hat{\lambda}_\alpha^2\frac{\partial\hat{\sigma}_\alpha}{\partial\hat{\lambda}_\alpha} + \hat{\sigma}_\alpha\hat{\lambda}_\alpha$, $\hat{\lambda}^{1-s}\hat{\lambda}_\alpha^{s+1}\,g_1$
$f_4 = \hat{\sigma}_\alpha\hat{\lambda}_\alpha$, $\hat{\sigma}\,\hat{\lambda}^{1-s}\hat{\lambda}_\alpha^{s}$
iiii. Extra terms related to non-affine:
$g_1 = \frac{\partial\hat{\sigma}}{\partial\hat{\lambda}}\,d_1 + (1-s)\,\frac{\hat{\sigma}}{\hat{\lambda}}\,d_1 + s\,\frac{\hat{\sigma}}{\hat{\lambda}_\alpha}$
$d_1 = \hat{\lambda}^{1-s}A\left[\hat{\lambda}_\alpha^{s-1}\right]$

2.6. Directionalisation of the isotropic hyperelastic models

As illustrated in the previous Section 2.5, the unidirectional solution P_{ut} were considered as a directional stress $\hat{\sigma}_\alpha$ for the representative directions. Notwithstanding, there exists another approach to obtain the directional stress $\hat{\sigma}_\alpha$. In general, it is straightforward to directionalise the invariant based isotropic hyperelastic models. To this end, firstly, the first isochoric invariant $\widehat{I}_1$ can be directionalised without effort by the relation of the constraint

$$A\left[\mathbf{e}_\alpha\otimes\mathbf{e}_\alpha\right] = \frac{1}{3}\mathbf{I}, \tag{26}$$

which can be obtained by analytical integration. The constraint in Eq. (26) has the advantage of being exactly satisfied when integrated with the Bažant and Oh (1986)'s integration points. Then, using Eq. (5), the first isochoric invariant $\widehat{I}_1$ takes the form

$$\widehat{I}_1 = \mathbf{I}:\hat{\mathbf{C}} = A\left[3\,\mathbf{e}_\alpha\otimes\mathbf{e}_\alpha:\hat{\mathbf{C}}\right] = A\left[3\,\hat{\lambda}_\alpha^2\right]. \tag{27}$$

In Kearsley (1989), the non-isochoric version of Eq. (27) was computed by the analytical integration of the squares of line segment stretch ratios $\lambda_\alpha^2 = \mathbf{F}\cdot\mathbf{e}_\alpha\cdot\mathbf{F}\cdot\mathbf{e}_\alpha$. Now, the following Neo–Hookean isochoric energy density function is considered

$$\rho_R\Phi^{iso} = \mu\left(\widehat{I}_1 - 3\right). \tag{28}$$

Then, insertion of Eq. (27) into the Neo–Hookean strain density function in Eq. (28), it yields to

$$\rho_R\Phi^{iso} = A\left[3\,\mu\left(\hat{\lambda}_\alpha^2 - 1\right)\right]. \tag{29}$$

Eq. (29) reflects the principal stretch based representation of the Neo–Hookean model by Rivlin and Taylor (1948). Consequently, the directional free energy $\rho_R\Phi_\alpha^{iso}$ is defined as

$$\rho_R\Phi_\alpha^{iso} = 3\,\mu\left(\hat{\lambda}_\alpha^2 - 1\right). \tag{30}$$

In comparison to the directional stress $\hat{\sigma}_\alpha$ in Eq. (24), Eq. (30) leads to a non-negative directional stress

$$\hat{\sigma}_\alpha = 6\,\mu_1\,\hat{\lambda}_\alpha. \tag{31}$$

The directional stress $\hat{\sigma}_\alpha$ in Eq. (31) is not zero for $\hat{\lambda}_\alpha = 1$, but after inserting it into Eqs. (16) and (17), the undeformed reference configuration is stress-free. Furthermore, it results in non-negative f_1, f_2, f_3 and f_4 values in Table 1. The non-negativity of the term f_2 arising from the so-called strong-ellipticity requirements, see Marsden and Hughes (1994), was discussed by Dal et al. (2018b). Only focusing on the isochoric response, based on Antman (1995) and Walton and Wilber (2003), the strong-ellipticity requirement is here postulated as

$$A\left[\mathbf{a}\otimes\mathbf{b}:\frac{\partial\left(\mathbf{F}\cdot\hat{\mathbf{S}}_\alpha\right)}{\partial\mathbf{F}}:\mathbf{a}\otimes\mathbf{b}\right] > 0 \tag{32}$$

$$\text{with}\quad \gamma = J(\mathbf{F}) - 1 \approx 0, \tag{33}$$

where $\mathbf{a}$ and $\mathbf{b}$ are non-zero unit vectors, and γ is the incompressibility constraint. According to Walton and Wilber (2003), for a small perturbation of the constraint γ, it must hold:

$$\left.\frac{\mathrm{d}}{\mathrm{d}\epsilon}\right|_{\epsilon=0} J(\mathbf{F}+\epsilon\,\mathbf{a}\otimes\mathbf{b}) = J\mathbf{F}^{-T} : \mathbf{a}\otimes\mathbf{b} \approx 0. \tag{34}$$

Using Eqs. (5) and (17) together with the strong-ellipticity requirements in Eqs. (32)–(34), after a lengthy calculation, the necessary constraint can be obtained as

$$A\left[J^{-\frac{2}{3}}\frac{\hat{\sigma}_\alpha}{\hat{\lambda}_\alpha}(\mathbf{b}\cdot\mathbf{e}_\alpha)^2 + J^{-\frac{4}{3}} f_2 (\mathbf{a}\cdot\mathbf{F}\cdot\mathbf{e}_\alpha)^2 (\mathbf{b}\cdot\mathbf{e}_\alpha)^2\right] > 0, \tag{35}$$

where the term f_2 is given in Table 1. Therefore, if the following relations hold in each representative direction, the strong-ellipticity is ensured:

$$\hat{\sigma}_\alpha > 0 \quad \text{and} \quad \frac{\partial\hat{\sigma}_\alpha}{\partial\hat{\lambda}_\alpha} \geqslant \frac{\hat{\sigma}_\alpha}{\hat{\lambda}_\alpha} > 0. \tag{36}$$

Based on the constraint in Eq. (36), it could be stated that the directional isochoric tangent modulus $\hat{\mathbb{C}}_\alpha$ arising from any directional stress $\hat{\sigma}_\alpha$ should satisfy non-negative f_1, f_2, f_3 and f_4 values. For this reason, care should be taken with the directional stress $\hat{\sigma}_\alpha$ in Eq. (24) in FE simulations.

Carol et al. (2004) (see also Verron, 2015) utilised the so-called solid angle $\mathrm{d}\,\omega$

$$\mathrm{d}\,\omega = \hat{\lambda}_\alpha^{-3}\,\mathrm{d}\,\Omega = \hat{\lambda}_\alpha^{-3}\,\sin\vartheta\,\mathrm{d}\,\vartheta\,\mathrm{d}\,\varphi \tag{37}$$

to obtain the trace of the inverse $\hat{\mathbf{C}}^{-1}$ and the isochoric second invariant $\widehat{I}_2$. Thus, the directional energy of the Mooney-Rivlin model yields to

$$\rho_R\,\Phi_\alpha^{iso} = 3\,\mu_1\left(\hat{\lambda}_\alpha^2 - 1\right) + 3\,\mu_2\left(\frac{1}{\hat{\lambda}_\alpha^5} - 1\right), \tag{38}$$

which was considered by Verron (2015). The corresponding directional stress $\hat{\sigma}_\alpha$ follows as

$$\hat{\sigma}_\alpha = 6\,\mu_1\,\hat{\lambda}_\alpha - \frac{15\,\mu_2}{\hat{\lambda}_\alpha^6}. \tag{39}$$

Eq. (39) is conditionally stable similar to Eq. (24). To elaborate, depending on a deformation state, Eq. (35) may or may not be satisfied due the violation of the directional constraint given in Eq. (36). Hence, instead of Eq. (38), two alternative approaches are considered. Firstly, an auxillary stretch $\hat{\hat{\lambda}}_\alpha$ can be defined as

$$\hat{\hat{\lambda}}_\alpha^4 = \mathbf{e}_\alpha\otimes\mathbf{e}_\alpha : \hat{\mathbf{C}}\cdot\hat{\mathbf{C}}. \tag{40}$$

With Eqs. (5) and (40), the isochoric second invariant $\widehat{I}_2$ yields to

$$\widehat{I}_2 = \frac{1}{2}\left(\widehat{I}_1^2 - \hat{\mathbf{C}}\cdot\hat{\mathbf{C}} : \mathbf{I}\right) = A\left[\frac{9}{2}A\left[\hat{\lambda}_\alpha^2\right]\hat{\lambda}_\alpha^2 - \frac{3}{2}\hat{\hat{\lambda}}_\alpha^4\right]. \tag{41}$$

Secondly, the so-called isochoric macro-area-stretch of Miehe et al. (2004) $\hat{\nu}_\alpha$, which is inverse of the distortional microplane thickening stretch $\bar{\lambda}_D = \frac{1}{\hat{\nu}_\alpha}$, can be considered:

$$\hat{\nu}_\alpha^2 = \mathbf{e}_\alpha\otimes\mathbf{e}_\alpha : \hat{\mathbf{C}}^{-1}. \tag{42}$$

Then, with the help of Eq. (49), the isochoric second invariant $\widehat{I}_2$ follows as

$$\widehat{I}_2 = A\left[3\,\hat{\nu}_\alpha^2\right]. \tag{43}$$

Similar to Eq. (27), Eq. (43) is in parallel with the result of Kearsley (1989). Thus, from Eqs. (41) and (43), the following relation holds

$$\hat{\nu}_\alpha^2 = \frac{3}{2}A\left[\hat{\lambda}_\alpha^2\right]\hat{\lambda}_\alpha^2 - \frac{1}{2}\hat{\hat{\lambda}}_\alpha^4. \tag{44}$$

Analogous to the derivation of Eq. (30), the Mooney-Rivlin isochoric free energy $\rho_R\,\Phi_\alpha^{iso}$ can be expressed as

$$\rho_R\,\Phi_\alpha^{iso} = 3\,\mu_1\left(\hat{\lambda}_\alpha^2 - 1\right) + 3\,\mu_2\left(\frac{3}{2}A\left[\hat{\lambda}_\alpha^2\right]\hat{\lambda}_\alpha^2 - \frac{1}{2}\hat{\hat{\lambda}}_\alpha^4 - 1\right). \tag{45}$$

Alternatively, by making use of Eq. (43), Eq. (45) takes a much simpler form

$$\rho_R\,\Phi_\alpha^{iso} = 3\,\mu_1\left(\hat{\lambda}_\alpha^2 - 1\right) + 3\,\mu_2\left(\hat{\nu}_\alpha^2 - 1\right). \tag{46}$$

Consequently, in combination to $\hat{\sigma}_\alpha$ given in Eq. (31), the additional isochoric directional stress $\hat{\hat{\sigma}}_\alpha$ due to the Mooney-Rivlin model is given as

$$\hat{\hat{\sigma}}_\alpha = \rho_R\frac{\partial\Phi_\alpha^{iso}}{\partial\hat{\hat{\lambda}}_\alpha} = 6\,\mu_2\left(\frac{3}{2}\left(A\left[\hat{\lambda}_\alpha\right]\hat{\lambda}_\alpha^2 + A\left[\hat{\lambda}_\alpha^2\right]\hat{\lambda}_\alpha\right) - \hat{\hat{\lambda}}_\alpha^3\right). \tag{47}$$

To obtain Eq. (47), the mathematical property $\left(A\left[\hat{\lambda}_\alpha^2\right]\right)^2 = A\left[A\left[\hat{\lambda}_\alpha^2\right]\hat{\lambda}_\alpha^2\right]$ is used. Moreover, considering the directional free energy in Eq. (46), the additional isochoric directional stress $\hat{\sigma}_\alpha^\nu$ can be represented as

$$\hat{\sigma}_\alpha^\nu = \rho_R\frac{\partial\Phi_\alpha^{iso}}{\partial\hat{\nu}_\alpha} = 6\,\mu_2\,\hat{\nu}_\alpha. \tag{48}$$

The directional stresses $\hat{\hat{\sigma}}_\alpha$ in Eq. (47) or $\hat{\sigma}_\alpha^\nu$ in Eq. (48) together with $\hat{\sigma}_\alpha$ given in Eq. (31) provide the representation of the Mooney-Rivlin model exactly, when integrated with any set of integration points satisfying the constraint

$$\sum_{\alpha=1}\mathbf{e}_\alpha\otimes\mathbf{e}_\alpha\,w_\alpha = \frac{1}{3}\mathbf{I}. \tag{49}$$

The stretch definitions $\hat{\hat{\lambda}}_\alpha$ and $\hat{\nu}_\alpha$ entail the modification of Eqs. (13) and (17). For this purpose, the time derivatives of $\hat{\hat{\lambda}}_\alpha$ and $\hat{\nu}_\alpha$ are required:

$$\dot{\hat{\hat{\lambda}}}_\alpha = \frac{1}{\hat{\hat{\lambda}}_\alpha^3}\,\mathbf{e}_\alpha\otimes\mathbf{e}_\alpha\cdot\dot{\hat{\mathbf{C}}} : \frac{1}{2}\dot{\hat{\mathbf{C}}}, \tag{50}$$

$$\dot{\hat{\nu}}_\alpha = -\frac{1}{\hat{\nu}_\alpha}\,\hat{\mathbf{C}}^{-1}\cdot\mathbf{e}_\alpha\otimes\mathbf{e}_\alpha\cdot\hat{\mathbf{C}}^{-1} : \frac{1}{2}\dot{\hat{\mathbf{C}}}. \tag{51}$$

Thus, the additional 2nd PK stress tensors are formulated as

$$\hat{\hat{\mathbf{S}}}_\alpha = J^{-\frac{2}{3}}\left(\frac{\hat{\hat{\sigma}}_\alpha}{\hat{\hat{\lambda}}_\alpha^3}\,\mathbf{e}_\alpha\otimes\mathbf{e}_\alpha\cdot\hat{\mathbf{C}} - \frac{1}{3}\hat{\sigma}_\alpha\hat{\hat{\lambda}}_\alpha\hat{\mathbf{C}}^{-1}\right), \tag{52}$$

$$\hat{\mathbf{S}}_\alpha^\nu = -J^{-\frac{2}{3}}\left(\frac{\hat{\sigma}_\alpha^\nu}{\hat{\nu}_\alpha}\,\hat{\mathbf{C}}^{-1}\cdot\mathbf{e}_\alpha\otimes\mathbf{e}_\alpha\cdot\hat{\mathbf{C}}^{-1} - \frac{1}{3}\hat{\sigma}_\alpha^\nu\hat{\nu}_\alpha\hat{\mathbf{C}}^{-1}\right). \tag{53}$$

With the additional stress contribution from Eqs. (52) and (53), the isochoric part of the 2nd PK stress tensor in Eq. (16) is remodified as

$$\hat{\mathbf{S}} = A\left[\hat{\mathbf{S}}_\alpha + \mathbf{A}\right], \tag{54}$$

where the additional stress contribution $\mathbf{A}$ can be considered as $\hat{\mathbf{S}}_\alpha^\nu$. The additional tangent modulus $\hat{\mathbb{C}}_\alpha^\nu = 2\,\frac{\partial\hat{\mathbf{S}}_\alpha^\nu}{\partial\hat{\mathbf{C}}}$ for Eq. (21) is

$$\hat{\mathbb{C}}^{v}_{\alpha} = -\frac{1}{3}\hat{J}^{\frac{2}{3}} f^{v}_{1}\left(\mathbf{C}^{-1}\cdot\mathbf{e}_{\alpha}\otimes\mathbf{e}_{\alpha}\cdot\mathbf{C}^{-1}\otimes\mathbf{C}^{-1} - \mathbf{C}^{-1}\otimes\mathbf{e}_{\alpha}\otimes\mathbf{e}_{\alpha}:\frac{\partial\mathbf{C}^{-1}}{\partial\mathbf{C}}\right) - \hat{J}^{\frac{4}{3}} f^{v}_{2}\left(\mathbf{C}^{-1}\cdot\mathbf{e}_{\alpha}\otimes\mathbf{e}_{\alpha}\cdot\mathbf{C}^{-1}\otimes\mathbf{e}_{\alpha}\otimes\mathbf{e}_{\alpha}:\frac{\partial\mathbf{C}^{-1}}{\partial\mathbf{C}}\right) + 2\hat{J}^{\frac{2}{3}} \times \frac{\hat{\sigma}^{v}_{\alpha}}{\hat{v}_{\alpha}}\,\mathrm{sym}\left(\mathbf{C}^{-1}\otimes\mathbf{C}^{-1}\cdot\mathbf{e}_{\alpha}\otimes\mathbf{e}_{\alpha}\cdot\mathbf{C}^{-1} + \mathbf{C}^{-1}\cdot\mathbf{e}_{\alpha}\otimes\mathbf{e}_{\alpha}\cdot\mathbf{C}^{-1}\otimes\mathbf{C}^{-1}\right) + \frac{1}{9} f^{v}_{3}\mathbf{C}^{-1}\otimes\mathbf{C}^{-1} + \frac{2}{3} f^{v}_{4}\frac{\partial\mathbf{C}^{-1}}{\partial\mathbf{C}}, \tag{55}$$

where $f^{v}_{1} = \frac{\hat{\sigma}^{v}_{\alpha}}{\hat{v}_{\alpha}} + \frac{\partial\hat{\sigma}^{v}_{\alpha}}{\partial\hat{v}_{\alpha}}$, $f^{v}_{2} = \frac{1}{\hat{v}^{2}_{\alpha}}\frac{\partial\hat{\sigma}^{v}_{\alpha}}{\partial\hat{v}_{\alpha}} - \frac{\hat{\sigma}^{v}_{\alpha}}{\hat{v}^{3}_{\alpha}}$, $f^{v}_{3} = \hat{v}^{2}_{\alpha}\frac{\partial\hat{\sigma}^{v}_{\alpha}}{\partial\hat{v}_{\alpha}} + \hat{\sigma}^{v}_{\alpha}\hat{v}_{\alpha}$, $f^{v}_{4} = \hat{\sigma}^{v}_{\alpha}\hat{v}_{\alpha}$ and $\mathrm{sym}(\cdot) = \frac{1}{2}\left((\cdot) + (\cdot)^{23^{T}}\right)$. Concerning the strong-ellipticity, in a similar manner with Eq. (35), the additional restriction owing to the isochoric macro-area-stretch $\hat{v}_{\alpha}$ can be calculated as

$$A\left[\hat{J}^{\frac{4}{3}} f^{v}_{2}\left(\mathbf{a}\cdot\mathbf{F}^{-T}\cdot\mathbf{e}_{\alpha}\right)^{2}\left(\mathbf{b}\cdot\mathbf{C}^{-1}\cdot\mathbf{e}_{\alpha}\right)^{2} + \hat{J}^{\frac{2}{3}}\frac{\hat{\sigma}^{v}_{\alpha}}{\hat{v}_{\alpha}}\left(\mathbf{a}\cdot\mathbf{F}^{-T}\cdot\mathbf{e}_{\alpha}\right)^{2}\left(\mathbf{F}^{-T}\cdot\mathbf{b}\right)^{2}\right] > 0, \tag{56}$$

where $f^{v}_{2} = \frac{1}{\hat{v}^{2}_{\alpha}}\frac{\partial\hat{\sigma}^{v}_{\alpha}}{\partial\hat{v}_{\alpha}} - \frac{\hat{\sigma}^{v}_{\alpha}}{\hat{v}^{3}_{\alpha}}$. Thus, together with Eq. (36), the necessary requirement to ensure the strong-ellipticity in each representative direction follows as

$$\hat{\sigma}^{v}_{\alpha} > 0 \quad \text{and} \quad \frac{\partial\hat{\sigma}^{v}_{\alpha}}{\partial\hat{v}_{\alpha}} \geqslant \frac{\hat{\sigma}^{v}_{\alpha}}{\hat{v}_{\alpha}} > 0. \tag{57}$$

Based on Eqs. (36) and (57), the Mooney-Rivlin directional energies in Eqs. (45) and (46) are unconditionally stable.

To avoid additional stress tensor computations due to Eq. (54), a simplified form of the directional energy depending only on $\hat{\sigma}_{\alpha}$ can be utilised. Then, by replacing $A\left[\hat{\lambda}^{2}_{\alpha}\right]$ with $\hat{\lambda}^{2}_{\alpha}$, and $\hat{\lambda}^{4}_{\alpha}$ with $\hat{\lambda}^{4}_{\alpha}$ in Eq. (45), the Mooney-Rivlin type directional energy is defined as

$$\rho_{R}\Phi^{iso}_{\alpha} = 3\,\mu_{1}\left(\hat{\lambda}^{2}_{\alpha} - 1\right) + 3\,\mu_{2}\left(\hat{\lambda}^{4}_{\alpha} - 1\right). \tag{58}$$

Hence, the directional stress $\hat{\sigma}_{\alpha}$ based on Eq. (58) can be obtained as

$$\hat{\sigma}_{\alpha} = 6\,\mu_{1}\,\hat{\lambda}_{\alpha} + 12\,\mu_{2}\left(\hat{\lambda}^{3}_{\alpha}\right). \tag{59}$$

In contrast to Eqs. (24) and (39), the directional stress $\hat{\sigma}_{\alpha}$ in Eq. (59) is stable due to the fulfillment of the strong-ellipticity condition in Eq. (36).

As a further example, the directionalisation procedure will be applied to Yeoh, Gent and the extended-tube models. The reason to select these models is due to the common applicability and their high performances on Treloar's data based on the work of Marckmann and Verron (2006). In general, the directional stresses are acquired by making use of the relation $\rho_{R}\dot{\Phi}^{iso} = \frac{\partial\Phi^{iso}}{\partial\widehat{I}_{1}}\dot{\widehat{I}}_{1} + \frac{\partial\Phi^{iso}}{\partial\widehat{I}_{2}}\dot{\widehat{I}}_{2} = A\left[\hat{\sigma}_{\alpha}\dot{\hat{\lambda}}_{\alpha} + \hat{\sigma}^{v}_{\alpha}\dot{\hat{v}}_{\alpha}\right]$. Then, with the help of $\dot{\widehat{I}}_{1} = A\left[6\hat{\lambda}_{\alpha}\dot{\hat{\lambda}}_{\alpha}\right]$ and $\dot{\widehat{I}}_{2} = A\left[6\hat{v}_{\alpha}\dot{\hat{v}}_{\alpha}\right]$, the directional stresses are defined as $\hat{\sigma}_{\alpha} = 6\hat{\lambda}_{\alpha}\rho_{R}\frac{\partial\Phi^{iso}}{\partial\widehat{I}_{1}}$ and $\hat{\sigma}^{v}_{\alpha} = 6\hat{v}_{\alpha}\rho_{R}\frac{\partial\Phi^{iso}}{\partial\widehat{I}_{2}}$. Now, firstly, the isochoric hybrid free energy of the Yeoh model is

$$\rho_{R}\Phi^{iso} = \mu_{1}\left(\widehat{I}_{1} - 3\right) + \mu_{2}\left(\widehat{I}_{1} - 3\right)^{2} + \mu_{3}\left(\widehat{I}_{1} - 3\right)^{3}. \tag{60}$$

The corresponding directional stress $\hat{\sigma}_{\alpha}$ follows as

$$\hat{\sigma}_{\alpha} = 6\,\hat{\lambda}_{\alpha}\left(\mu_{1} + 2\,\mu_{2}\left(\widehat{I}_{1} - 3\right) + 3\,\mu_{3}\left(\widehat{I}_{1} - 3\right)^{2}\right). \tag{61}$$

Secondly, the isochoric hybrid free energy of the Gent model can be expressed as

$$\rho_{R}\Phi^{iso} = -\mu_{1}(I_{m} - 3)\,\ln\frac{I_{m} - \widehat{I}_{1}}{I_{m} - 3}, \tag{62}$$

where I_{m} is related to the maximum stretch limit. This limit must not be exceeded to avoid numerical problems. The directional stress $\hat{\sigma}_{\alpha}$ is

$$\hat{\sigma}_{\alpha} = 6\,\mu_{1}\,\hat{\lambda}_{\alpha}\,\frac{I_{m} - 3}{I_{m} - \widehat{I}_{1}}. \tag{63}$$

According to Marckmann and Verron (2006), the extended-tube model of Kaliske and Heinrich (1999) performs best to describe Treloar's data. For this reason, this model is also considered for the directionalisation. Due to the definition of the tube part in the original model, approximate directionalisation is carried out by making use of the isochoric macro-area-stretch $\hat{v}_{\alpha}$ (i.e. $\hat{\sigma}^{v}_{\alpha} = \rho_{R}\frac{\partial\Phi^{iso,tube}_{\alpha}}{\partial\hat{v}_{\alpha}}$). The isochoric hybrid free energy of the extended-tube type model is considered as

$$\rho_{R}\Phi^{iso} = \mu_{c}\left[\frac{(1-\delta^{2})\left(\widehat{I}_{1} - 3\right)}{1 - \delta^{2}\left(\widehat{I}_{1} - 3\right)} + \ln\left(1 - \delta^{2}\left(\widehat{I}_{1} - 3\right)\right)\right] + A\left[\frac{2\,\mu_{e}}{\beta}\left(\hat{v}^{2\beta}_{\alpha} - 1\right)\right]. \tag{64}$$

Subsequently, the directional stresses are

$$\hat{\sigma}_{\alpha} = 6\,\mu_{c}\,\hat{\lambda}_{\alpha}\left[\frac{1-\delta^{2}}{\left(1 - \delta^{2}\left(\widehat{I}_{1} - 3\right)\right)^{2}} - \frac{\delta^{2}}{1 - \delta^{2}\left(\widehat{I}_{1} - 3\right)}\right] \text{ and } \hat{\sigma}^{v}_{\alpha} = 4\,\mu_{e}\hat{v}^{2\beta-1}_{\alpha}. \tag{65}$$

2.7. An ad hoc approach to improve integration points

The integration weights and directions computed by Bažant and Oh (1986) can be specifically tailored to each model. There are many different sets of integration points in the literature overviewed in detail by Verron (2015) and Itskov (2016). From a practical point of view, the most important consideration when optimising the integration points is the fulfilment of the material symmetry, see Ehret et al. (2010). Hence, to improve the material symmetry, a rotational scheme is devised as illustrated in Fig. 2. The goal of the rotational scheme is to load the unit-sphere along all possible direction vectors of the employed numerical integration scheme. According to this approach, the unit-sphere is rotated for each and all discrete direction vectors aligning with the chosen main direction (e.g. $\mathbf{e}_{3}$). Moreover, the unit-sphere can be further rotated around the $\mathbf{e}_{3}$ direction to provide more rotational effects. Table 2 demonstrates the optimisation procedure in detail based

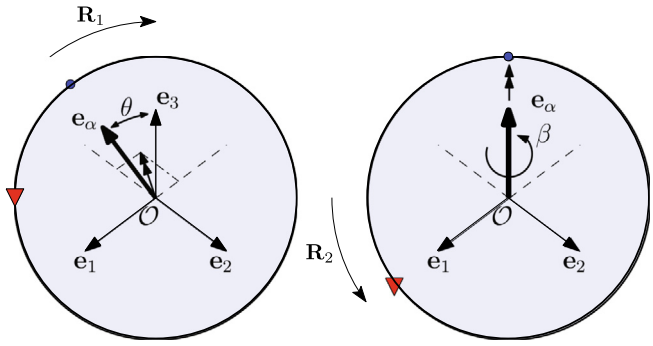

Fig. 2. Each representative direction is rotated around the basis $\mathbf{e}_{\alpha}\times\mathbf{e}_{3}$ by the amount of θ, then around $\mathbf{e}_{\alpha}$ by the amount of β to provide more rotational effects.

on the rotational scheme illustrated in Fig. 2. As a note, the direction vectors can be also predefined, but this is not taken into account, as they are distributed rather well. As an alternative, for instance, Gauss points can be utilised with a suitable domain transformation. However, as pointed out by Bažant and Oh (1986), they are not uniformly distributed on the unit-sphere and localised around the pole. Hence, the integration weights can be optimised instead of the representative directions. In this case, the optimisation problem is classified as a highly constrained linear optimisation problem or the so-called linear programming (see Luenberger and Ye, 2015). To solve this sort of optimisation problems, MATLAB provides the robust *lsqlin* function.

3. Numerical examples

3.1. Comparisons of Lion's model

In this part, two homogenous stress states, namely uniaxial tension (UT) and equibiaxial-tension (ET), are considered to compare the directional stress $\hat{\sigma}_\alpha$ of Lion et al. (2013) in Eq. (24) and the non-affine directional stress $\hat{\sigma}$ in Eq. (25). The algorithm shown in Table 3 is utilised without computing the tangent modulus $\mathbb{C}$. The employed 2nd PK stress tensors for the computations are given in Eq. (17) for the affine model and in Eq. (18) for the non-affine model. The simulated results are based on the integration points of Fliege and Maier (1999) in parallel with Itskov (2016), as these integration points were utilised to compute the reference numerical solution.

Firstly, for the UT case with $J = 1$, the isochoric right Cauchy-Green deformation tensor is given as

$$\hat{\mathbf{C}} = \frac{1}{\lambda}\,\mathbf{e}_1 \otimes \mathbf{e}_1 + \frac{1}{\lambda}\,\mathbf{e}_2 \otimes \mathbf{e}_2 + \lambda^2\,\mathbf{e}_3 \otimes \mathbf{e}_3. \tag{66}$$

Table 2
An ad hoc optimisation strategy for the improvement of integration weights for material symmetry. s_f is 2 for symmetric points, otherwise 1.

i. Given the experimental data
the representative directions $\mathbf{e}_\alpha$
$\mathbf{P}_{ut}$, $\mathbf{P}_{et} = [P_1, P_2, \dots P_m]^T$,
$\boldsymbol{\lambda} = [\lambda_1, \lambda_2, \dots \lambda_m]^T$, $\hat{\mathbf{C}}(\lambda)$
ii. For each $\mathbf{e}_\gamma$, where $\gamma = 1, \dots, n_r$,
compute $\mathbf{R}^\gamma = \mathbf{R}_2 \cdot \mathbf{R}_1$
1. $\bar{\mathbf{e}}_\gamma = \frac{\mathbf{e}_\gamma \times \mathbf{e}_3}{\|\mathbf{e}_\gamma \times \mathbf{e}_3\|}$, $cos\theta = \mathbf{e}_\gamma \cdot \mathbf{e}_3$, $sin\theta = \|\bar{\mathbf{e}}_\gamma\|$,
2. $\mathbf{R}_1 = \bar{\mathbf{e}}_\gamma \otimes \bar{\mathbf{e}}_\gamma + \cos\theta(\mathbf{I} - \bar{\mathbf{e}}_\gamma \otimes \bar{\mathbf{e}}_\gamma) + \sin\theta\,\bar{\mathbf{e}}_\gamma \times \mathbf{I}$
3. $\mathbf{R}_2 = \mathbf{e}_3 \otimes \mathbf{e}_3 + \cos\beta(\mathbf{I} - \mathbf{e}_3 \otimes \mathbf{e}_3) + \sin\beta\,\mathbf{e}_3 \times \mathbf{I}$
iii. For each computed rotation tensor $\mathbf{R}^\gamma$
compute the $\mathbf{A}^\gamma$ matrix
for $i = 1 : m$
for $\alpha = 1 : n_{dir}$
1. $\mathbf{e}^* = \mathbf{R}^\gamma \cdot \mathbf{e}_\alpha$, $\hat{\lambda}_\alpha = \sqrt{\mathbf{e}^* \cdot \hat{\mathbf{C}} \cdot \mathbf{e}^*}$
2. $\hat{\sigma}_\alpha$ from the 1D constitutive law
3. $\hat{\mathbf{S}}_\alpha = \frac{\hat{\sigma}_\alpha}{\hat{\lambda}_\alpha}\,\mathbf{e}_\alpha \otimes \mathbf{e}_\alpha - \frac{1}{3}\,\hat{\sigma}_\alpha\,\hat{\lambda}_\alpha\,\hat{\mathbf{C}}^{-1}$
4. *if* uniaxial
$A^\gamma_{i\alpha} = s_f * 1.5\,\lambda_i\,\hat{S}_{33,\alpha}$
elseif equibiaxial
$A^\gamma_{i\alpha} = s_f * 3\,\lambda_i\,\hat{S}_{11,\alpha}$
iv. Form the complete $\boldsymbol{A}$ and $\boldsymbol{d}$ matrix
$\boldsymbol{A} = \left[c^1\boldsymbol{A}^1, c^2\boldsymbol{A}^2, \dots, c^{n_{dir}}\boldsymbol{A}^{n_{dir}}\right]^T$ $\boldsymbol{d} = \left[c^1\boldsymbol{P}, c^2\boldsymbol{P}, \dots, c^{n_{dir}}\boldsymbol{P}\right]^T$
v. Optimise the weights $\boldsymbol{w} = [w_1, \dots, w_n]^T$
$\min_{\boldsymbol{w}} \frac{1}{2}\,\|\boldsymbol{A}\boldsymbol{w} - \boldsymbol{d}\|^2$,
with constraints $\boldsymbol{lb} \leqslant \boldsymbol{w} \leqslant \boldsymbol{ub}$,
$\sum_{\alpha=1} \mathbf{e}_\alpha w_\alpha = 0$ and
$\sum_{\alpha=1} \mathbf{e}_\alpha \otimes \mathbf{e}_\alpha w_\alpha = \frac{1}{3}\,\boldsymbol{I}$

Table 3
An algorithm for the computation of the isochoric 2nd PK stress tensor $\hat{\mathbf{S}}$ and the isochoric tangent modulus $\hat{\mathbb{C}}$ at each local Gauss point in the reference configuration.

Given: $\mathbf{e}_\alpha, w_\alpha, \hat{\mathbf{C}}$
Initialise: $\hat{\mathbf{S}} = 0$ and $\hat{\mathbb{C}} = 0$
Compute:
Non-affine: $\hat{\lambda} = \left(\sum_{\alpha=1}^{n_r} w_\alpha\,\hat{\lambda}_\alpha^p\right)^{1/s}$, $\hat{\sigma}\left(\hat{\lambda}\right)$
for $\alpha = 1 : n_{dir}$
$\hat{\lambda}_\alpha = \sqrt{\mathbf{e}_\alpha \otimes \mathbf{e}_\alpha : \hat{\mathbf{C}}}$, $\hat{v}_\alpha = \sqrt{\mathbf{e}_\alpha \otimes \mathbf{e}_\alpha : \hat{\mathbf{C}}^{-1}}$
$\hat{\sigma}_\alpha\left(\hat{\lambda}_\alpha\right), \hat{\sigma}^v_\alpha(\hat{v}_\alpha)$
$\hat{\mathbf{S}}_\alpha$ (Eq. (17) or Eq. (18)), $\hat{\mathbf{S}}^v_\alpha$ (Eq. (53))
$\hat{\mathbb{C}}_\alpha$ (Table 1), $\hat{\mathbb{C}}^v_\alpha$ (Eq. (55)
$\hat{\mathbf{S}} = \hat{\mathbf{S}} + w_\alpha\left(\hat{\mathbf{S}}_\alpha + \hat{\mathbf{S}}^v_\alpha\right)$
$\hat{\mathbb{C}} = \hat{\mathbb{C}} + w_\alpha\left(\hat{\mathbb{C}}_\alpha + \hat{\mathbb{C}}^v_\alpha\right)$

The 1st PK stress P_{ut} vs the stretch λ of both the affine and the non-affine approach for two different sets of material parameters are depicted in Fig. 3. The stiffening effect of the non-affine approach is observed with the increasing values of s in Fig. 3. However, for the compression (i.e. $\hat{\lambda} < 1$), this effect is smaller compared to tension. For $s = 100$, the non-affine solutions in both cases are close to the unidirectional stress in Eq. (22). Nevertheless, high values of s are inadmissible as Eq. (8) then approaches the infinity norm.

Secondly, in the case of ET, the isochoric right Cauchy-Green deformation tensor is given as

$$\hat{\mathbf{C}} = \lambda^2\,(\mathbf{e}_1 \otimes \mathbf{e}_1 + \mathbf{e}_2 \otimes \mathbf{e}_2) + \frac{1}{\lambda^4}\,\mathbf{e}_3 \otimes \mathbf{e}_3. \tag{67}$$

The 1st PK stress P_{et} vs the stretch λ of the affine and non-affine approach for two different parameter cases are illustrated in Fig. 4. In a similar trend with the UT case, the stiffening effect of the non-affine approach can also be observed with increasing values of s in Fig. 4. However, unlike the UT, the stiffening effect of the non-affine approach is relatively small. In other words, the unidirectional solution is difficult to obtain, even with the high values of s.

3.2. Parameter identification of the directionalised models

Here, the main objective is to assess the directionalised forms presented in Section 2.6 with the Treloar's data. To do that, for example, the material parameters (here denoted as the original parameters) from Marckmann and Verron (2006) or Hossain and Steinmann (2013) can be employed, as they are optimised for Treloar's data. After computing the unidirectional stress P_{uni} (P_{ut} and P_{et}) with these parameters, a parameter fit is done with the *lsqnonlin* and the *ga* functions of MATLAB. The function *ga* is considered for the Yeoh, the Gent and the extended-tube type model since *lsqnonlin* can get stuck in a local optimum. The parameters for these three models are identified based on the digitised data of Treloar tabulated in Hossain and Steinmann (2013). For the numerical integration, the 21 integration points of Bažant and Oh (1986) are used as listed in Table 5. The original parameters of the models and the identification results are given in Table 4,5.

Firstly, the results for the approximated Mooney-Rivlin type model are shown in Fig. 5. Furthermore, Lion et al. (2013)'s directional stress in Eq. (24) can be optimised for the Mooney-Rivlin original parameters shown in Table 4. The comparisons are displayed in Fig. 6. Secondly, the Yeoh model is considered. The parameter identification results are shown in Fig. 7. Thirdly, the Gent model is displayed in Fig. 8. Finally, the extended-tube type

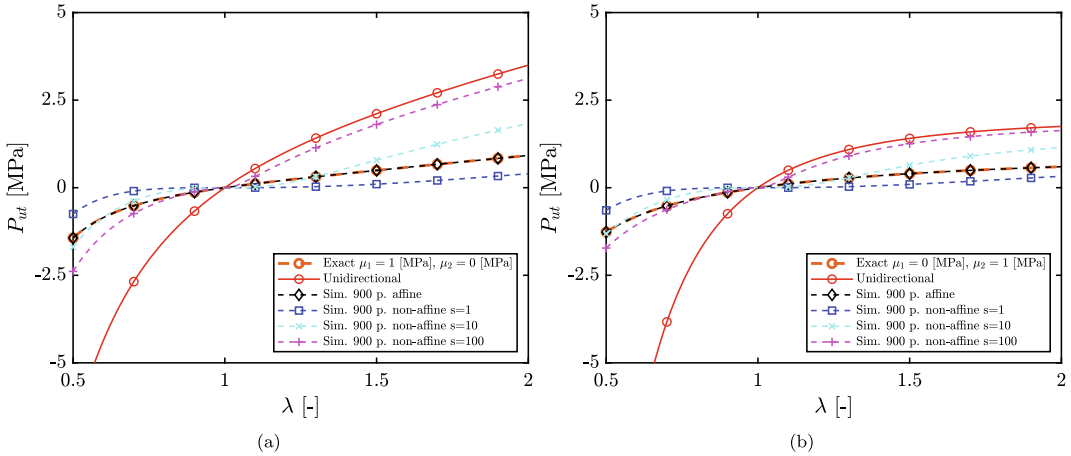

Fig. 3. The comparisons of the affine and non-affine models for the UT case. The exact solution is based on the analytical integration of Eq. (24) by Lion et al. (2013). For the non-affine computations, Eq. (25) is employed. (a) $\mu_1 = 1$ [MPa] and $\mu_2 = 0$ [MPa] (b) $\mu_1 = 0$ [MPa] and $\mu_2 = 1$ [MPa].

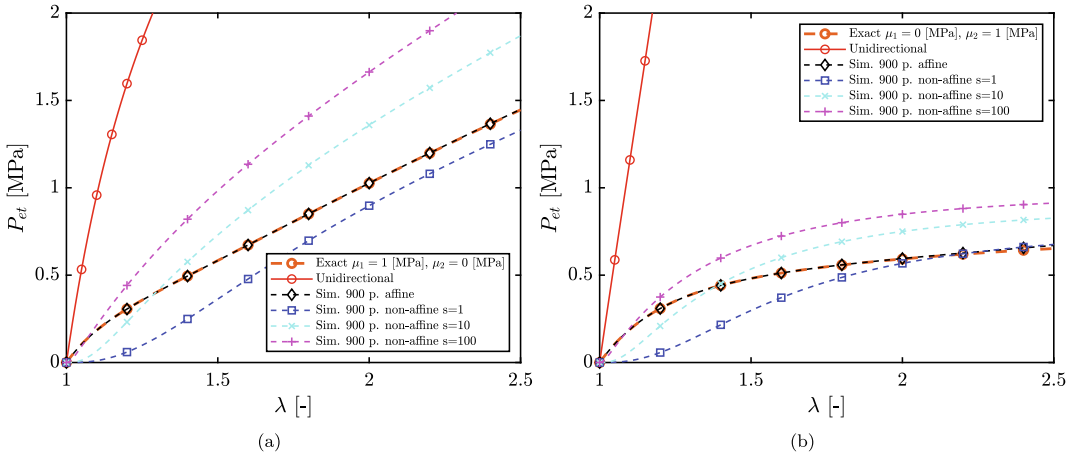

Fig. 4. The comparisons of the affine and non-affine models for the ET case. The exact solution is based on the analytical integration of Eq. (24) by Lion et al. (2013). For the non-affine computations, Eq. (25) is employed. (a) $\mu_1 = 1$ [MPa] and $\mu_2 = 0$ [MPa] (b) $\mu_1 = 0$ [MPa] and $\mu_2 = 1$ [MPa].

Table 4
The original and identified model parameters for the directionalisation comparisons.

Mooney-Rivlin	μ_1[MPa]	μ_2[MPa]		
Original	0.1620	5.90e−3		
UT	0.170	~ 0		
ET	0.1617	3.56e−3		
Lion	μ_1[MPa]	μ_2[MPa]		
UT	0.1085	0.6868		
ET	0.6026	~ 0		
Yeoh	μ_1[MPa]	μ_2[MPa]	μ_3[MPa]	
UT	0.1643	−1.53e−3	4.32e−5	
ET	0.2132	−1.27e−3	3.95e−5	
Gent	μ_1[MPa]	I_m		
UT	0.1229	82.6		
ET	0.1809	114.1		
Extended-tube	μ_c[MPa]	δ	μ_e[MPa]	β
UT	0.0974	9.15e−3	0.300	0.172
ET	0.1402	7.47e−3	0.129	0.064

model fits are plotted in Fig. 9. In the cases of approximated version of the Mooney-Rivlin model in Fig. 5 and the model of Lion et al. (2013) in Fig. 6, small to moderate differences in comparison with the corresponding standard Mooney-Rivlin solution exist. As a remark, the model applied by Lion et al. (2013) is not formulated using the directionalisation of the classical Mooney-Rivlin strain energy as applied here. The Yeoh and Gent models are exactly directionalised, and these models are not able to fit the UT and ET data together. In this aspect, the extended-tube type model performs better than the mentioned models. This particular success stems from the directionalisation of the tube term in Eq. (64) with the isochoric macro-area-stretch $\hat{v}_\alpha$.

3.3. Optimisation of the integration points

Based on the algorithm demonstrated in Table 2, the 21 integration weights of Bažant and Oh (1986) are optimised for the analytical solutions of Lion et al. (2013) for the UT and ET cases. As an optimisation tool, MATLAB's *lsqlin* function is utilised. For the optimisation of the weights for the UT, the following vector $\mathbf{d}$ is considered:

$$\mathbf{d} = \left[\underbrace{\mathbf{P}_{ut}, \ldots, \mathbf{P}_{ut}}_{\mu_1=1,\,\mu_2=0}, \underbrace{\mathbf{P}_{ut}, \ldots, \mathbf{P}_{ut}}_{\mu_1=0,\,\mu_2=1} \right]^T , \tag{68}$$

where the size of vector $\mathbf{d}$ is $2 \times n_{\text{dir}} \times m$, and m is the length of the analytical solution $\mathbf{P}_{ut}$ from Lion et al. (2013). Moreover, under-

Table 5
Optimised integration weigths for the 21 points, w_B represents Bažant and Oh (1986)'s weights. w_{ut} and w_{et} are based on the optimisation for UT and ET, respectively.

α	$e_{\alpha 1}$	$e_{\alpha 2}$	$e_{\alpha 3}$	w_B	w_{ut}	w_{et}
1	0	0	1	0.0265214244093	0.0251909960250	0.0238695589281
2	0	1	0	0.0265214244093	0.0251909960250	0.0238695589281
3	1	0	0	0.0265214244093	0.0251909960250	0.0238695589281
4	0	0.707106781187	0.707106781187	0.0199301476312	0.0222769709304	0.0238018297263
5	0	−0.707106781187	0.707106781187	0.0199301476312	0.0222769709304	0.0238018297263
6	0.707106781187	0	0.707106781187	0.0199301476312	0.0222769709304	0.0238018297263
7	−0.707106781187	0	0.707106781187	0.0199301476312	0.0222769709304	0.0238018297263
8	0.707106781187	0.707106781187	0	0.0199301476312	0.0222769709304	0.0238018297263
9	−0.707106781187	0.707106781187	0	0.0199301476312	0.0222769709304	0.0238018297263
10	0.836095596749	0.387907304067	0.387907304067	0.0250712367487	0.0242304321952	0.0238018297263
11	−0.836095596749	0.387907304067	0.387907304067	0.0250712367487	0.0242304321952	0.0238018297263
12	0.836095596749	−0.387907304067	0.387907304067	0.0250712367487	0.0242304321952	0.0238018297263
13	−0.836095596749	−0.387907304067	0.387907304067	0.0250712367487	0.0242304321952	0.0238018297263
14	0.387907304067	0.836095596749	0.387907304067	0.0250712367487	0.0242304321952	0.0238018297263
15	−0.387907304067	0.836095596749	0.387907304067	0.0250712367487	0.0242304321952	0.0238018297263
16	0.387907304067	−0.836095596749	0.387907304067	0.0250712367487	0.0242304321952	0.0238018297263
17	−0.387907304067	−0.836095596749	0.387907304067	0.0250712367487	0.0242304321952	0.0238018297263
18	0.387907304067	0.387907304067	0.836095596749	0.0250712367487	0.0242304321952	0.0238018297263
19	−0.387907304067	0.387907304067	0.836095596749	0.0250712367487	0.0242304321952	0.0238018297263
20	0.387907304067	−0.387907304067	0.836095596749	0.0250712367487	0.0242304321952	0.0238018297263
21	−0.387907304067	−0.387907304067	0.836095596749	0.0250712367487	0.0242304321952	0.0238018297263

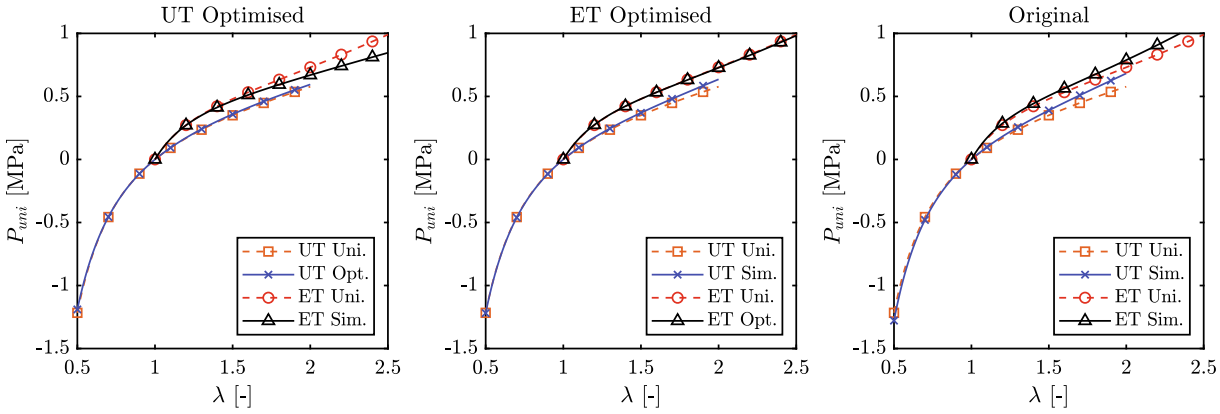

Fig. 5. The comparisons for the approximately directionalised version of the Mooney-Rivlin model in Eq. (59) with the unidirectional solutions of the standard Mooney-Rivlin model.

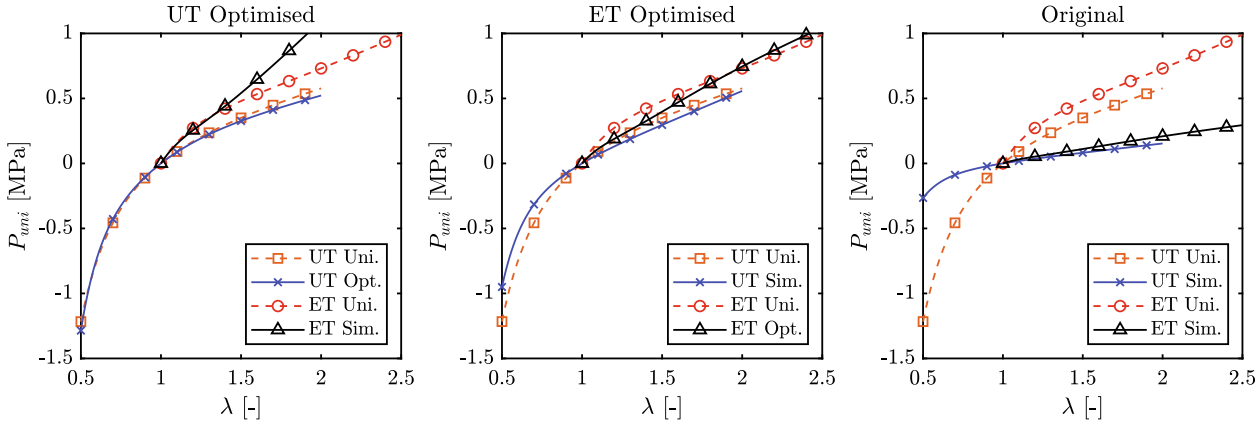

Fig. 6. The parameter identification results for the model of Lion et al. (2013).

braces indicate the evaluated $\mathbf{P}_{ut}$ for that parameter set. Similarly, for the ET case, $\mathbf{d}$ is defined as

$$\mathbf{d} = \left[\underbrace{\mathbf{P}_{et}, \ldots, \mathbf{P}_{et}}_{\mu_1=1,\,\mu_2=0}, \underbrace{\mathbf{P}_{et}, \ldots, \mathbf{P}_{et}}_{\mu_1=0,\,\mu_2=1} \right]^T . \tag{69}$$

The directional stresses from the directionalisation of the Mooney-Rivlin model in Section 2.6 are not considered for the optimisation since they do represent the Mooney-Rivlin model exactly. In this regard, the exact solutions of Lion et al. (2013) provide a solid setting for any numerical comparison.

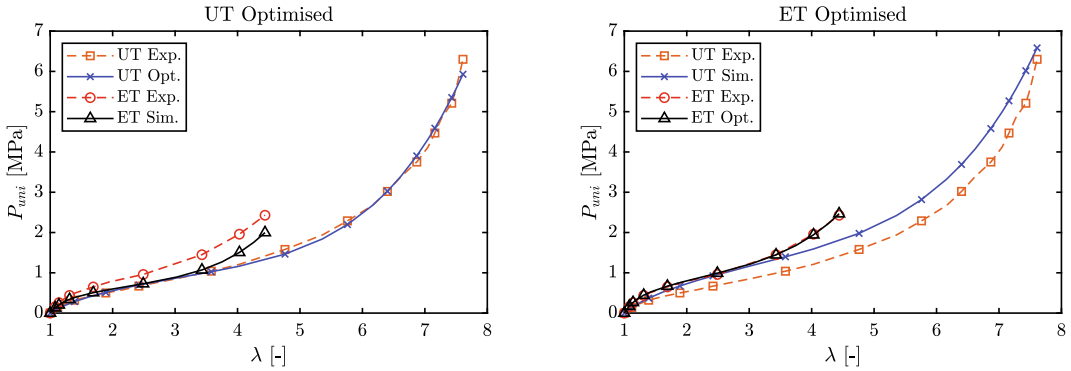

Fig. 7. The parameter identification results for the Yeoh model given by Eq. (61).

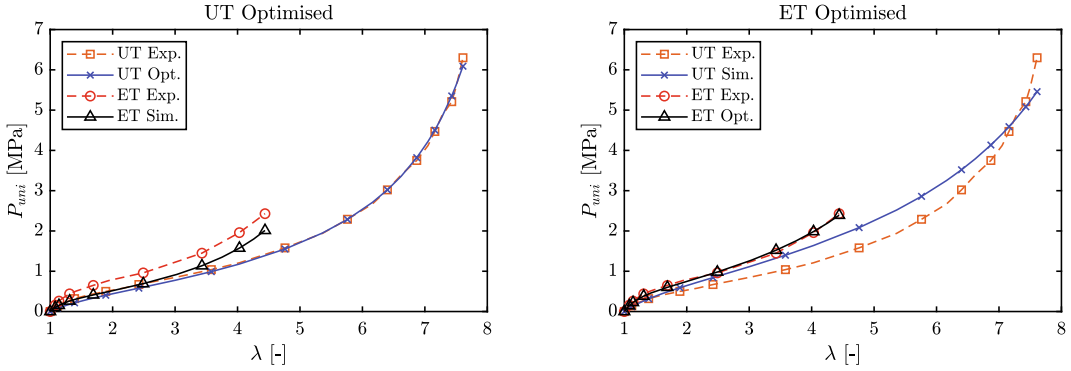

Fig. 8. The parameter identification results for the Gent model given by Eq. (63).

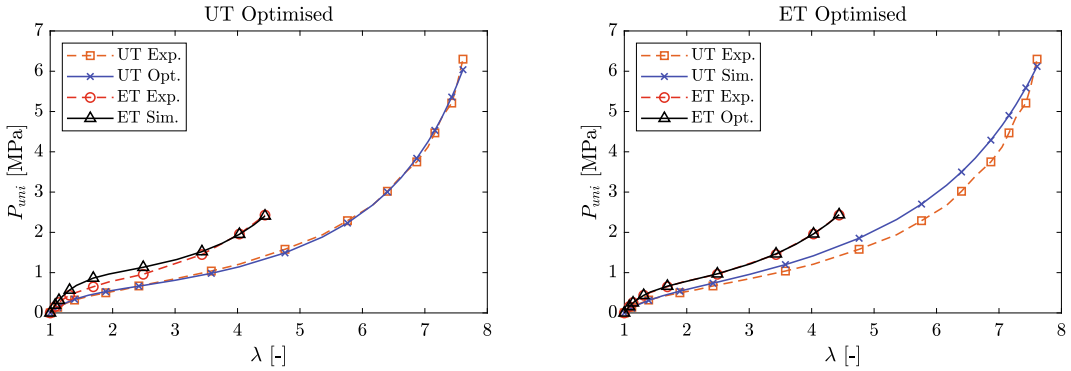

Fig. 9. The parameter identification results for the extended-tube type model given by Eq. (65).

First, the optimisation is done for the UT vector **d** given in Eq. (68). Subsequently, the optimisation results are visualised in Fig. 10. Since 21 integration points are considered, the unit-sphere is rotated 21 times according to the algorithm. Essentially, each loading curve represents the corresponding rotation. Therefore, this visualisation manifests material symmetry. Another technique to assess material symmetry is the annular disk benchmark of Ehret et al. (2010). However, to observe the changes in material symmetry, the locking stretch of the corresponding microsphere model has to be reached. For this reason, it is not considered in this study. This matter was discussed in Dal et al. (2018b). Based on Fig. 10, it can be concluded that the algorithm given in Table 2 slightly improves the material symmetry. Although the integration weights are optimised for the UT, the optimisation of material symmetry for the ET is more obvious.

Second, the optimisation results for the ET vector **d** given in Eq. (69) are displayed in Fig. 11. In this case, despite the optimisation is based on the ET, there is no significant difference between the UT results in Fig. 11 with the UT results in Fig. 10. Considering the ET case, a clear improvement of material symmetry is observed since the loading curves closely cluster around each other. The optimised weights for the UT and ET are listed in Table 5.

3.4. FE benchmark 1: perforated strip with a hole

In this part, a perforated strip with a hole is analysed. The main motivation of this benchmark is to compare different 1D stress-stretch relations for a non-homogeneous stress state in contrast to the UT and ET cases. The FE program COMSOL is used to analyse the directional models given in Sections 2.5 and 2.6. Furthermore,

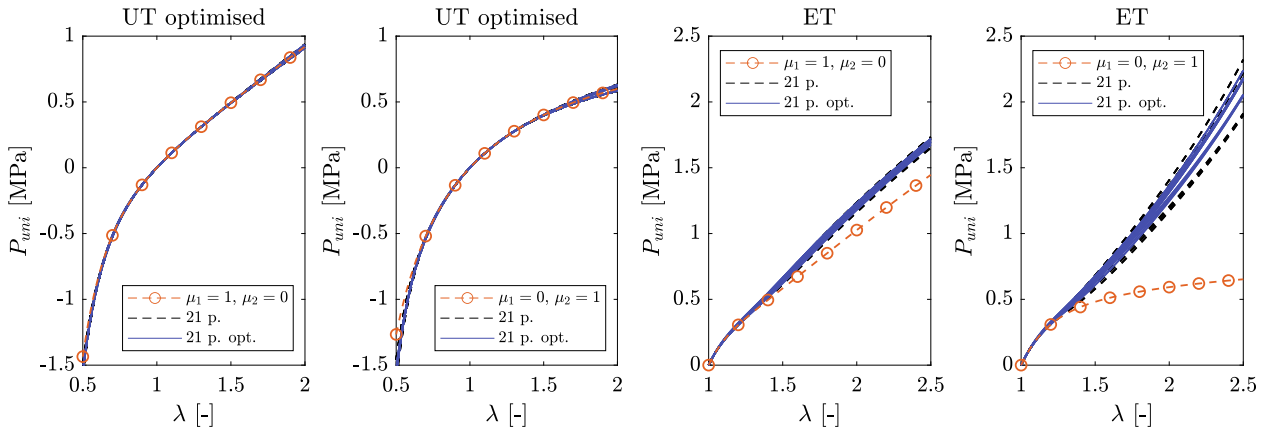

Fig. 10. The optimisation of Bažant and Oh (1986)'s 21 point weights for the UT. The ET results are recomputed based on the optimised weights.

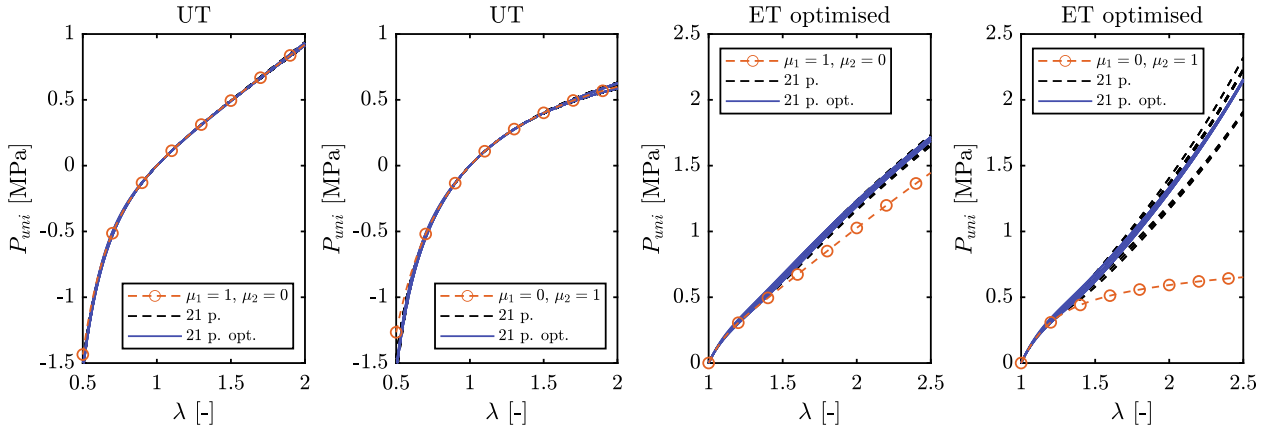

Fig. 11. The optimisation results of the Bažant and Oh (1986)'s 21 Points. The points are optimised based on the exact solutions of the ET and recomputed for the UT.

since incompressibility has to be taken into account, the mixed u-p approach is applied to overcome the inherent numerical difficulties. Hence, the perturbed Lagrangian method (see Sussman and Bathe, 1987) with constant pressure is a natural choice for the hybrid free energy approach. Due to the volumetric energy defined in Eq. (15) in Section 2.3 (e.g. $\rho_R \Phi^{vol} = \frac{\kappa}{2}(J-1)^2$), there is no difference between the formulation used here with the Q1P0 formulation by Simo et al. (1985) and Miehe (1994). To begin with, the following Galerkin form is considered:

$$G(\mathbf{u}, p, \delta\mathbf{u}, \delta p) = \int_{\mathscr{B}_R^e} \mathbf{S} : \delta\mathbf{E}\, dV + \int_{\mathscr{B}_R^e} \delta p \left(J - 1 + \frac{p}{K}\right) dV = 0. \qquad (70)$$

The geometry and boundary conditions are illustrated in Fig. 12. For this standard geometry, the dimensions are obtained from Waffenschmidt et al. (2014). Fig. 13 depicts the norm of the total displacement $||\mathbf{u}||$ and the Von-Mises stresses $\sqrt{\frac{3}{2}\mathbf{T}^D : \mathbf{T}^D}$ for the Mooney-Rivlin type model in Eq. (59) (cf. Eq. (31) and (48) for the exact form). Furthermore, the directional stresses $\hat{\sigma}_\alpha$ of the two mentioned models are locally compared with each other at point A. The material parameters employed are from the ET fit given in Table 4. For both models, the results of the corresponding contour plots seem to be similar. On the other hand, the local directional stresses are different. Eq. (24) results in negative $\hat{\sigma}_\alpha$ values separately from Eq. (59), which produces positive values. Albeit their $\hat{\sigma}_\alpha$ definitions are different, the $\hat{\sigma}_\alpha$ curves have a similar trend. Furthermore, Eq. (24) depicts a slight numerical convergence problem associated with Eq. (36), when the loading is further increased. In contrast, Eq. (59) does not have numerical issues with further loading.

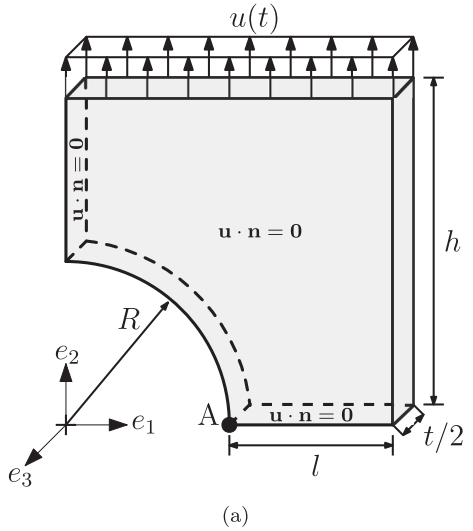

Fig. 12. (a) Perforated strip with a hole ($t = 20, h = 100, l = 50$ and $R = 50$), all in mm. Only the 1/8 of the geometry is analysed due to the geometric and boundary condition symmetries. The displacements are ramped up to 100 and 660 mm ($\lambda = 2$ and $\lambda = 7.6$) with 20 loading steps, 3600 Q1P0 elements with 6 elements per thickness.

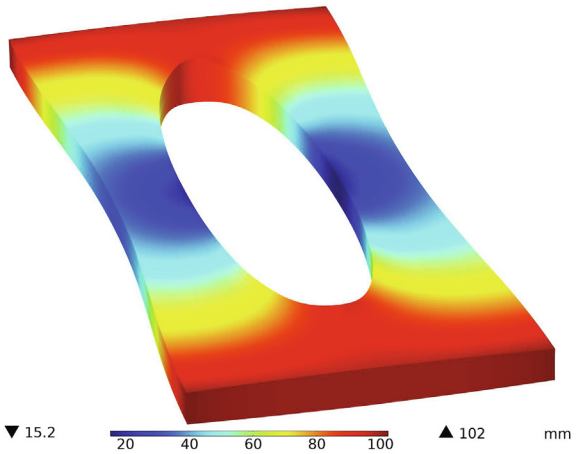

(a) LM, the total displacement $||\boldsymbol{u}||$

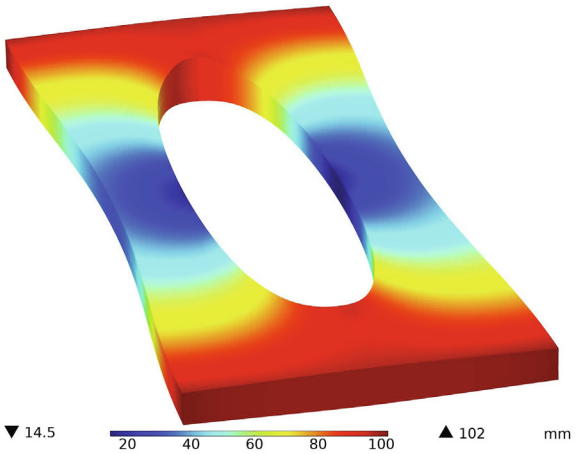

(b) AMRM, the total displacement $||\boldsymbol{u}||$

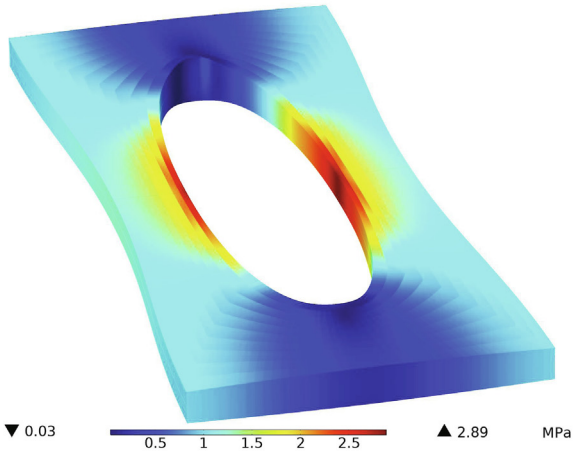

(c) LM, the Von-Mises stress $\sqrt{\frac{3}{2}\,\mathbf{T}^D : \mathbf{T}^D}$

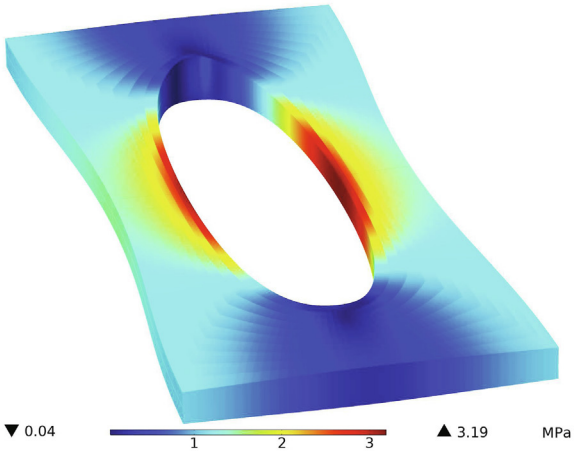

(d) AMRM, the Von-Mises stress $\sqrt{\frac{3}{2}\,\mathbf{T}^D : \mathbf{T}^D}$

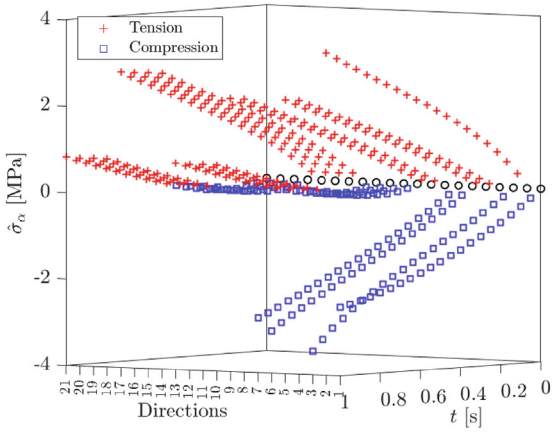

(e) LM, directional stresses $\hat{\sigma}_\alpha$ at point A

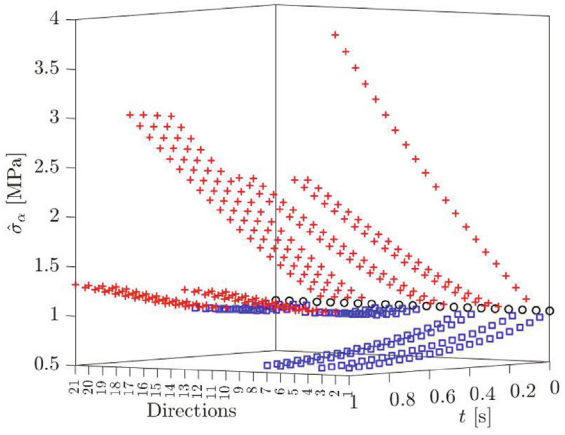

(f) AMRM, directional stresses $\hat{\sigma}_\alpha$ at point A

Fig. 13. The comparisons between models of Lion et al. (2013) in Eq. (24) and Mooney-Rivlin type model given in Eq. (59).

To compare the directionalised models in a quantitative sense, force–displacement curves are considered. The employed parameters are chosen for the ET case given in Table 4. However, UT parameters are employed for the Yeoh, Gent and extended-tube type models, as the loading strech of $\lambda = 7.6$ is considered. Moreover, for the Mooney-Rivlin model defined by Eqs. (31) and (48), which is essentially equivalent to the standard Mooney-Rivlin model, the original parameters in Table 4 are employed. The results are demonstrated in Fig. 14. Firstly, based on the optimisation results presented in the previous Section 3.3, optimised integration weights are compared with each other utilising the directional stress of Lion et al. (2013) in Eq. (24). According to Fig. 14, employing different integration weights does not affect the results. As a further remark, the variation of μ_2 affects the results only slightly,

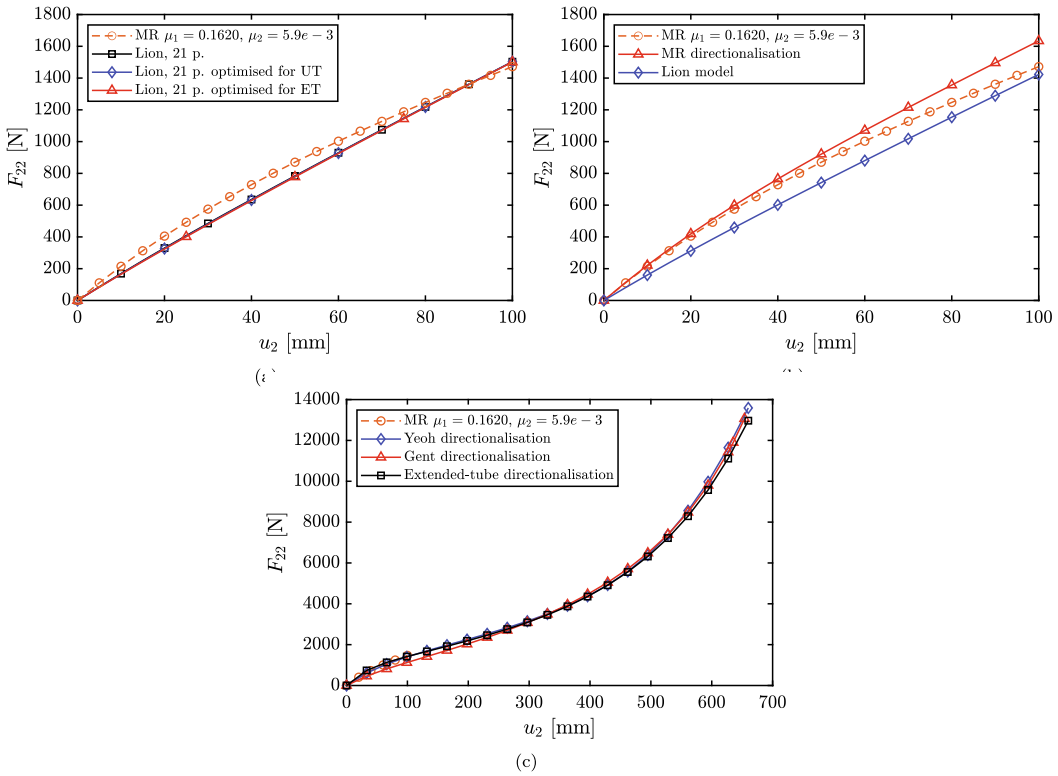

Fig. 14. The force–displacement curves. Forces are multiplied with four due to the symmetry. (a) The evaluation of different sets of integration weights for the model of Lion et al. (2013) is based on Table 5 (b) a comparison of Lion et al. (2013) (Eq. 24) and Mooney-Rivlin type (Eq. 59) models (c) A comparison of Yeoh (Eq. 61), Gent (Eq. 63) and extended-tube type (Eq. 65) models from Section 2.6 for strains up to $\lambda = 7.6$.

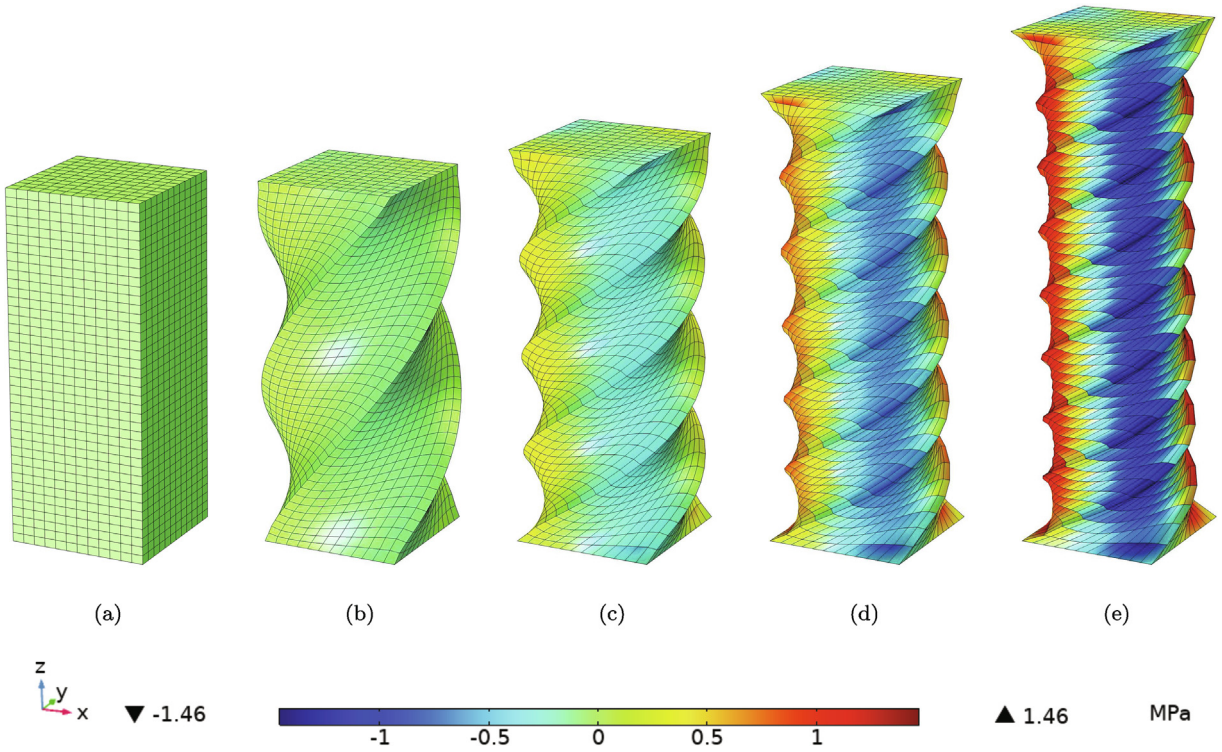

Fig. 15. The T^D_{12} component of the deviatoric Cauchy stress tensor $\mathbf{T}^D$ for the Lion's model in Eq. (24). (a) $\phi = 0$ (b) $\phi = \pi$ (c) $\phi = 2\pi$ (d) $\phi = 3\pi$ (e) $\phi = 4\pi$. The material parameters employed are from the ET fit given in Table 4.

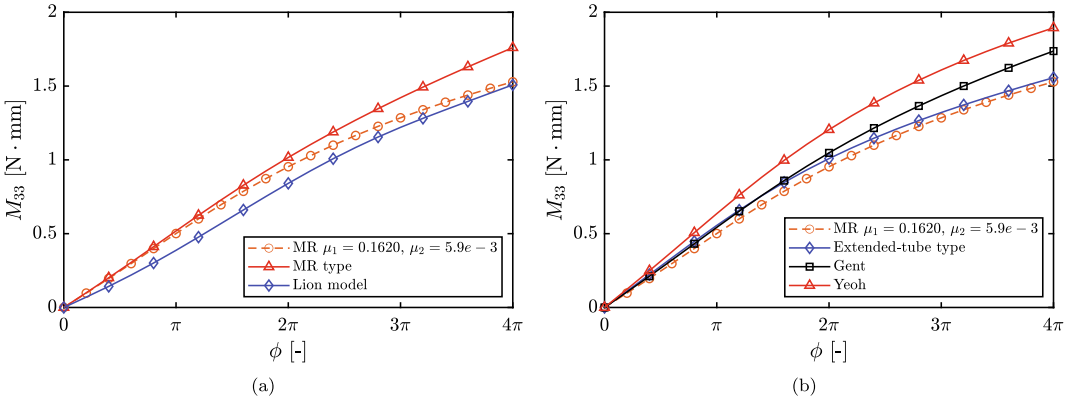

Fig. 16. The moment-rotation curves for the directional models presented in Sections 2.5 and 2.6. (a) A comparison of Lion et al. (2013) (Eq. 24) and Mooney-Rivlin type (Eq. 59) models (b) Comparisons between the Yeoh (Eq. 61), Gent (Eq. 63) and extended-tube type (Eq. 65) models. Moments M_{33} are calculated from the Cauchy stress **T**. The material parameters employed are from the ET fit given in Table 4.

as the nonlinearity is small. Furthermore, Fig. 14 elucidates the Yeoh (Eq. 61), Gent (Eq. 63) and extended-tube type (Eq. 65) models for large strains, in which they display a similar UT-like performance.

3.5. FE benchmark 2: twist of a rectangular prism

Another numerical example, which is inspired from Dal et al. (2018b), is presented to assess both the stability and the performance of the directional stress $\hat{\sigma}_\alpha$ of the directional models. Here, a rectangular prism ($2 \times 2 \times 5$ mm) with $12 \times 12 \times 40$ discontinuous pressure-linear displacement elements is subjected to 4π rotation on the top of the geometry. To rotate the top of the surface, a rigid connector is utilised. Moreover, at the centre of the top surface, u_1 and u_2 components of the displacement are fixed, but u_3 is left free. In total, 50 loading steps are considered. The moment M_{33} (evaluated in the actual configuration) and rotation ϕ are obtained from the RBE2 type formulation. In the simulations, no stability problems occurred, despite the extreme deformations. Quadratic convergence was observed for each loading step. The contour plots of the simulation are shown in Fig. 15. The displacement on the top surface is computed as $u_3 = 2.1058\,[\text{mm}]$. Similar to Section 3.4, the moment M_{33} and rotation ϕ comparisons are illustrated in Fig. 16. The moment-rotation curves depict mild nonlinearity. Furthermore, the differences between the Yeoh, Gent and extended-tube models are due to the parameter identification based on large strains.

4. Conclusion

For the affine and non-affine representative directions model, the same structure of the material modulus arises. The investigations of the non-affine approach have shown relatively unfeasible solutions compared to the affine approach. The directionalisation concept introduced here is a favourable alternative to statistical thermomechanics oriented approaches by obtaining 1D directional stresses from the standard first and second invariant based hyperelastic models. Furthermore, it provides a sound basis for inelastic modelling extensions. As an interesting outcome, it is possible to make standard invariant based isotropic models direction dependent. Moreover, with two different directional stretch definitions, the method results in an equivalent form of second Piola–Kirchhoff stress tensor acquired from the invariant based approach. If the inelasticity is included in the modelling, the related tensor mechanics and additional terms in the evolution equations due to the macro-area-stretch could be cumbersome. Thus, an approximate directionalisation can be combined with the multiplicative split of the micro-stretch. However, for a simultaneous UT and ET curve fitting, as in the case of extended-tube model, the inclusion of the macro-area-stretch is essential. In general, the employment of the UT solution of any hyperelastic model as a directional stress should be avoided. The presented algorithm for optimising the weights of the integration schemes reveals that improvement in material symmetry for initially isotropic materials can be obtained. Nonetheless, improvement of the accuracy was not observed. The FE benchmarks also illustrated that the force–displacement and moment-rotation curves are not affected by the change of integration weights. In future, this should be investigated further with microsphere based models. The extension of the algorithm is possible as integration directions and weights in the literature could be optimised for the intended application area.

Declaration of Competing Interest

The authors declare that they have no known competing financial interests or personal relationships that could have appeared to influence the work reported in this paper.

Acknowledgements

We hereby acknowledge the financial support by Universität der Bundeswehr München. We thank to anonymous reviewers for their insightful comments.

References

Antman, S., 1995. Nonlinear Problems of Elasticity..
Bažant, P., Oh, B.H., 1986. Efficient numerical integration on the surface of a sphere. ZAMM – J. Appl. Math. Mech./Z. Angew. Math. Mech. 66, 37–49.
Bažant, Z., 1984. Microplane Model for Strain-controlled Inelastic Behaviour. Wiley, London, pp. 45–59.
Bažant, Z.P., Gambarova, P.G., 1984. Crack shear in concrete: crack band microflane model. J. Struct. Eng. 110, 2015–2035.
Bažant, Z.P., Oh, B.H., 1985. Microplane model for progressive fracture of concrete and rock. J. Eng. Mech. 111, 559–582.
Berger, T., Kaliske, M., 2020. A thermo-mechanical material model for rubber curing and tire manufacturing simulation. Comput. Mech. 66, 513–535.
Bleistein, T., Jung, A., Diebels, S., 2020. A microsphere-based material model for open cell metal foams. Continuum Mech. Thermodyn. 32, 255–267.
Carol, I., Jirásek, M., Bažant, Z., 2001. A thermodynamically consistent approach to microplane theory. Part I. Free energy and consistent microplane stresses. Int. J. Solids Struct. 38, 2921–2931.
Carol, I., Jirásek, M., Bažant, Z.P., 2004. A framework for microplane models at large strain, with application to hyperelasticity. Int. J. Solids Struct. 41, 511–557.
Dal, H., Cansız, B., Miehe, C., 2018a. A three-scale compressible microsphere model for hyperelastic materials. Int. J. Numer. Methods Eng. 116, 412–433.

Dal, H., Kaliske, M., 2009. A micro-continuum-mechanical material model for failure of rubber-like materials: application to ageing-induced fracturing. J. Mech. Phys. Solids 57, 1340–1356.
Dal, H., Zopf, C., Kaliske, M., 2018b. Micro-sphere based viscoplastic constitutive model for uncured green rubber. Int. J. Solids Struct. 132–133, 201–217.
Ehret, A.E., Itskov, M., Schmid, H., 2010. Numerical integration on the sphere and its effect on the material symmetry of constitutive equations—a comparative study. Int. J. Numer. Methods Eng. 81, 189–206.
Fliege, J., Maier, U., 1999. The distribution of points on the sphere and corresponding cubature formulae. IMA J. Numer. Anal. 19, 317–334.
Flory, P.J., 1961. Thermodynamic relations for high elastic materials. Trans. Faraday Soc. 57, 829–838.
Freund, M., Ihlemann, J., 2010. Generalization of one-dimensional material models for the finite element method. ZAMM – J. Appl. Math. Mech./Z. Angew. Math. Mech. 90, 399–417.
Guilié, J., Le, T.-N., Le Tallec, P., 2015. Micro-sphere model for strain-induced crystallisation and three-dimensional applications. J. Mech. Phys. Solids 81, 58–74.
Göktepe, S., Miehe, C., 2005. A micro–macro approach to rubber-like materials. Part iii: the micro-sphere model of anisotropic mullins-type damage. J. Mech. Phys. Solids 53, 2259–2283.
Haupt, P., 2000. Continuum Mechanics and Theory of Materials. Advanced Texts in Physics. Springer Berlin Heidelberg.
Hossain, M., Steinmann, P., 2013. More hyperelastic models for rubber-like materials: consistent tangent operators and comparative study. J. Mech. Behav. Mater. 22, 27–50.
Itskov, M., 2016. On the accuracy of numerical integration over the unit sphere applied to full network models. Comput. Mech. 57, 859–865.
Kaliske, M., Heinrich, G., 1999. An extended tube-model for rubber elasticity: statistical-mechanical theory and finite element implementation. Rubber Chem. Technol. 72, 602–632.
Kearsley, E.A., 1989. Note: strain invariants expressed as average stretches. J. Rheol. 33, 757–760.
Kuhl, E., Steinmann, P., Carol, I., 2001. A thermodynamically consistent approach to microplane theory. Part ii. Dissipation and inelastic constitutive modeling. Int. J. Solids Struct. 38, 2933–2952.
Lion, A., Diercks, N., Caillard, J., 2013. On the directional approach in constitutive modelling: a general thermomechanical framework and exact solutions for Mooney-Rivlin type elasticity in each direction. Int. J. Solids Struct. 50, 2518–2526.
Lion, A., Dippel, B., Liebl, C., 2014. Thermomechanical material modelling based on a hybrid free energy density depending on pressure, isochoric deformation and temperature. Int. J. Solids Struct. 51, 729–739.
Loos, K., Aydogdu, A.B., Lion, A., Johlitz, M., Calipel, J., 2020. Strain-induced crystallisation in natural rubber: a thermodynamically consistent model of the material behaviour using a multiphase approach. Continuum Mech. Thermodyn. 32, 501–526.
Loos, K., Aydogdu, A.B., Lion, A., Johlitz, M., Calipel, J., 2020. Strain-induced crystallisation in natural rubber: a thermodynamically consistent model of the material behaviour using a serial connection of phases. Continuum Mech. Thermodyn., 1–34
Luenberger, D., Ye, Y., 2015. Linear and Nonlinear Programming. International Series in Operations Research & Management Science. Springer International Publishing.
Marckmann, G., Verron, E., 2006. Comparison of hyperelastic models for rubber-like materials. Rubber Chem. Technol. 79, 835–858.
Marsden, J., Hughes, T., 1994. Mathematical Foundations of Elasticity..
Menzel, A., Waffenschmidt, T., 2009. A microsphere-based remodelling formulation for anisotropic biological tissues. Philos. Trans. Roy. Soc. A: Math., Phys. Eng. Sci. 367, 3499–3523.
Miehe, C., 1994. Aspects of the formulation and finite element implementation of large strain isotropic elasticity. Int. J. Numer. Methods Eng. 37, 1981–2004.
Miehe, C., Göktepe, S., Lulei, F., 2004. A micro-macro approach to rubber-like materials – Part I: the non-affine micro-sphere model of rubber elasticity. J. Mech. Phys. Solids 52, 2617–2660.
Miehe, C., Göktepe, S., 2005. A micro–macro approach to rubber-like materials. Part ii: the micro-sphere model of finite rubber viscoelasticity. J. Mech. Phys. Solids 53, 2231–2258.
Mistry, S.J., Govindjee, S., 2014. A micro-mechanically based continuum model for strain-induced crystallization in natural rubber. Int. J. Solids Struct. 51, 530–539.
Nateghi, A., Dal, H., Keip, M.A., Miehe, C., 2018. An affine microsphere approach to modeling strain-induced crystallization in rubbery polymers. Continuum Mech. Thermodyn. 30, 485–507.
Noll, W., Coleman, B.D., 1974. The Thermodynamics of Elastic Materials with Heat Conduction and Viscosity. The Foundations of Mechanics and Thermodynamics, pp. 145–156..
Pawelski, H., 1998. Erklärung einiger mechanischer Eigenschaften von Elastomerwerkstoffen mit Methoden der statistischen Physik. Berichte aus dem Maschinenbau. Shaker..
Rivlin, R.S., Taylor, G.I., 1948. Large elastic deformations of isotropic materials. i. Fundamental concepts. Philos. Trans. Roy. Soc. Lond. Ser. A Math. Phys. Sci. 240, 459–490.
Simo, J., Taylor, R., Pister, K., 1985. Variational and projection methods for the volume constraint in finite deformation elasto-plasticity. Comput. Methods Appl. Mech. Eng. 51, 177–208.
Sussman, T., Bathe, K.-J., 1987. A finite element formulation for nonlinear incompressible elastic and inelastic analysis. Comput. Struct. 26, 357–409.
Thylander, S., Menzel, A., Ristinmaa, M., 2017. A non-affine electro-viscoelastic microsphere model for dielectric elastomers: application to vhb 4910 based actuators. J. Intell. Mater. Syst. Struct. 28, 627–639.
Verron, E., 2015. Questioning numerical integration methods for microsphere (and microplane) constitutive equations. Mech. Mater. 89, 216–228.
Waffenschmidt, T., Polindara, C., Menzel, A., Blanco, S., 2014. A gradient-enhanced large-deformation continuum damage model for fibre-reinforced materials. Comput. Methods Appl. Mech. Eng. 268, 801–842.
Walton, J.R., Wilber, J., 2003. Sufficient conditions for strong ellipticity for a class of anisotropic materials. Int. J. Non-Linear Mech. 38, 441–455.